1
Computational Studies of Heteroatom-Assisted C–H Activation at Ru, Rh, Ir, and Pd as a Basis for Heterocycle Synthesis and Derivatization

Kevin J. T. Carr, Stuart A. Macgregor, and Claire L. McMullin

1.1
Introduction

Modern computational chemistry is a key tool by which insight into organometallic reaction mechanisms can be gained. The ability to characterize short-lived intermediates and transition states provides an ideal complement to experiment, where such information is often extremely difficult, if not impossible, to obtain. Recent years have seen great advances in understanding the mechanisms of C–H bond activation, and this area was the subject of several major reviews toward the end of the last decade [1, 2]. More recently, the focus has shifted to how C–H activation can be integrated into catalytic cycles for useful organic transformations. The C–H bond activation event is itself mechanistically diverse, with oxidative addition (OA), σ-bond metathesis (SBM), and electrophilic activation (EA) all potentially available at late transition metal centers, depending on the metal, its oxidation state, and the coordination environment. C–H activation assisted by a heteroatom base (typically a carboxylate or carbonate) falls into the last of these categories and forms the focus of this chapter. More recently, computational studies of catalytic cycles for C–H activation and functionalization have become more common. These reveal the complexity of what are usually multiple-step processes, and calculations are particularly well placed to test different mechanistic possibilities. Such studies are most effectively pursued through a close interaction between experiment and computation, and increasingly this is allowing for a more quantitative assessment of computed reaction mechanisms.

As well as progress in mechanistic understanding, the last 10 years have seen important developments in the computational methodologies available to model transition metal reactivity. While density functional theory (DFT) remains the core method of choice, the ability to model larger systems that more closely reflect experiment has highlighted the known shortcomings of DFT in describing dispersion interactions. These long-range, stabilizing interactions are individually weak, but their cumulative effect in large systems can be significant. Methods to incorporate this component include its separate calculation (e.g.,

with Grimme's D3 parameter set [3]), use of functionals that include a treatment of dispersion (e.g., B97-D [4], ωB97X-D [5]), or use of a Minnesota functional (e.g., M06 or its variants [6]) where the functional parameterization (e.g., to reproduce molecular structures from crystallographic data) captures dispersion effects without explicitly identifying them. The validity of such approaches is seen, for example, in marked improvements in calculated $L_nM\text{-}PR_3$ dissociation energies [7]. These developments make the choice of functional for the study of C–H activation and functionalization especially critical when larger models are employed in calculations.[1)]

This chapter will focus on how computational chemistry has provided insights into heteroatom-assisted C–H activation and functionalization at Ru, Rh, Ir, and Pd metal centers. These will include reactions that both construct new heterocycles and those that introduce new substituents into an already intact heterocyclic skeleton. The text will first cover Pd and will then treat Ru, Rh, and Ir together, providing in each case a brief background on computational work on heteroatom-assisted C–H activation. More recent developments will then be considered covering the literature since our last review [1b], that is, from 2009 until March 2015. In many cases, work on nonheterocyclic substrates is included to illustrate important general points regarding the C–H activation mechanism. Unless otherwise stated, DFT calculations have been employed throughout and only the major functional employed in each study will be highlighted, along with any solvent used in brackets. The notation DFT2//DFT1 will be used to indicate cases where a second functional (DFT2) has been used to recompute the energy of a system optimized with an initial functional (DFT1). The original papers should be consulted for full computational details.

1.2 Palladium

1.2.1 Intramolecular Heteroatom-Assisted C–H Activation

1.2.1.1 Early Computational Studies

Computational work under this heading stems from 2005 when Davies, Macgregor, and coworkers reported BP86 calculations on the cyclometalation of dimethylbenzylamine at $Pd(OAc)_2$ [8], a system that had been the subject of detailed experimental studies in the 1980s by Ryabov and coworkers (Figure 1.1) [9]. Starting from $Pd(OAc)_2(Me_2NCH_2Ph)$, **1**, a two-step process was characterized involving initial displacement of one arm of the κ^2-OAc ligand by the incoming *ortho*-C–H bond of the benzyl substituent. This forms an agostic intermediate, **2**, that polarizes the C–H bond and sets up an H-bond to the

1) High-level wavefunction methods promise the accurate treatment of these long-range electron correlation effects; however, such methods are still too computationally demanding for routine use on large model systems.

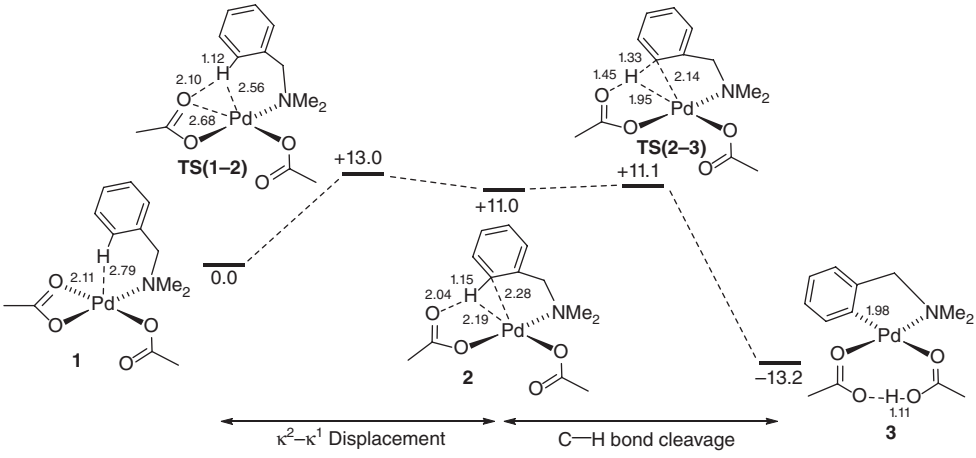

Figure 1.1 Computed reaction profile for C–H activation in $Pd(OAc)_2(Me_2NCH_2Ph)$. Energies are in kcal/mol and include a correction for zero-point energies; selected distances in Å [8].

pendant arm of the OAc ligand. C–H cleavage then proceeds with a minimal barrier to give the cyclometalated product, **3**, as an HOAc adduct. The overall barrier was computed to be 13 kcal mol^{-1} with the initial $\kappa^2-\kappa^1$ displacement of acetate via **TS(1–2)** corresponding to the highest point on the profile. Alternative mechanisms including oxidative addition or proton transfer onto the Pd-bound acetate oxygen were found to entail considerably higher barriers. The implication of an agostic intermediate, as opposed to a Wheland (or arenium)-type species, was significant as it indicates a fundamental difference to electrophilic aromatic substitution (S_EAr) processes. This type of reaction was subsequently characterized as proceeding via "ambiphilic metal–ligand assistance" (AMLA), a term that stresses the synergic role of the electron-deficient metal center and the nearby intramolecular base in promoting facile C–H bond activation [1b]. Both AMLA-6 and AMLA-4 processes have been defined, depending on whether a six-membered or four-membered transition state is involved. The role of an agostic intermediate indicates AMLA C–H activation is not (unlike S_EAr) restricted to aromatic C–H bonds, and indeed the equivalent $C(sp^3)$–H activation of $Me_2NCH_2CH_2CH_3$ was predicted to proceed with a barrier of only 20 kcal mol^{-1}.

Shortly afterward, Maseras, Echavarren, and coworkers published a B3LYP study on C–H activation in Pd(2-phenethylphenyl)(X)(PH_3) species (**4**, X = Br or HCO_3, Figure 1.2), as model intermediates in $Pd(OAc)_2$-catalyzed intramolecular C–C coupling [11]. The Pd–aryl bond is formed via oxidative addition of an aryl bromide precursor and acts as a directing group. With $X = HCO_3$, C–H activation proceeds by a one-step proton abstraction via **TS4A** in a similar way to that seen at $Pd(OAc)_2(Me_2NCH_2Ph)$, albeit without an agostic intermediate being located. With X = Br, proton abstraction was much less accessible; however, in this case, external deprotonation by a bicarbonate anion (**TS4B**) was found to

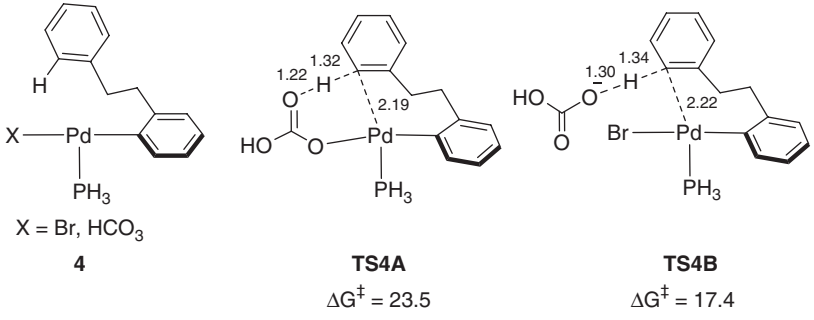

Figure 1.2 C–H activation transition states derived from **4**, involving internal (**TS4A**) and external (**TS4B**) deprotonation. Computed free energies in kcal mol^{-1} and key distances in Å [10].

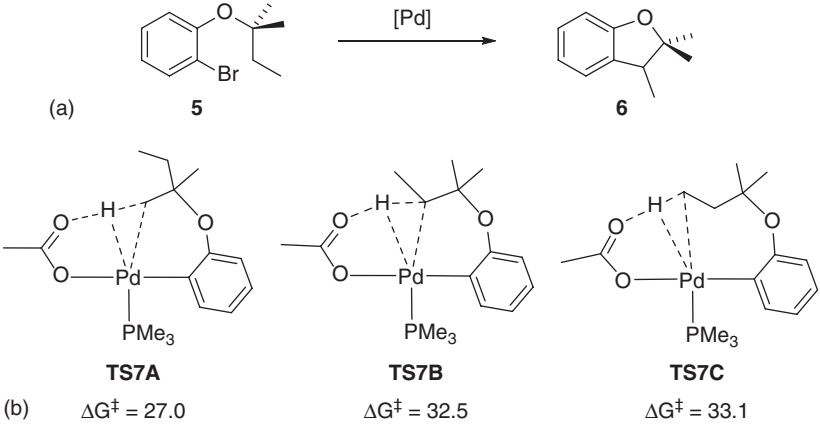

Figure 1.3 (a) Pd-catalyzed formation of dihydrobenzofurans and (b) alternative transition states for C(sp^3)–H activation with computed free energies relative to Pd(Ar)(OAc)(PMe$_3$), **7**, in kcal mol^{-1} [12].

be competitive. A follow-on study showed that both intra- and intermolecular deprotonation mechanisms correctly capture the accelerating effect of electron-withdrawing substituents (F, Cl) on the aryl ring, as seen experimentally [10]. Such patterns are again inconsistent with a S_EAr mechanism.

The importance of agostic interactions was also seen in the ability to cleave C(sp^3)–H bonds as part of the Pd-catalyzed synthesis of dihydrobenzofurans (**5** → **6**, Figure 1.3a) reported by Fagnou and coworkers [12]. B3LYP calculations on a model Pd(Ar)(OAc)(PMe$_3$) species, **7**, characterized a series of concerted, inner-sphere deprotonation mechanisms for reaction at the three distinct C(sp^3)–H bonds of the 2-methylbutoxy substituent (Figure 1.3b). Reaction at one of the Me positions that results in a six-membered palladacycle is favored via **TS7A** over activation of either the CH_2 or CH_3 groups of the ethyl substituent via **TS7B** and **TS7C**, respectively, the latter forming a seven-membered

palladacycle. These one-step C–H activation processes were consistent with the "concerted metalation deprotonation" (CMD) concept that Fagnou and coworkers were developing at this time. Lledós and Urriolabeitia found similar B3LYP-computed processes accounted for observed selectivities in the cyclometalation of stabilized iminophosphoranes, $Ar_3P{=}NC(O)Ph$ at $Pd(OAc)_2$, where *exo* activation via an agostic intermediate is kinetically favored over a one-step *endo* activation [13].

Overall, these early studies of carboxylate-assisted intramolecular C–H activation established the key features of these AMLA/CMD processes, where an electron-deficient metal center works in concert with a pendant carboxylate base to promote C–H activation. This is most evident when an agostic intermediate is involved and such species also rationalize how these systems can also perform C(sp^3)–H bond activation. Whether C–H activation is achieved as a one- or two-step process appears rather system dependent. Alternative mechanisms, for example, proton transfer onto a halide ligand, oxidative addition, or AMLA-4 processes involving proton transfer onto the inner (Pd-bound) oxygen of the carboxylate were all ruled out. Likewise, no evidence for S_EAr processes had been reported. Subsequent work was set against this background and considered the various other parameters that may affect the C–H bond activation process.

1.2.1.2 The Role of the Base, Solvent, and Additives on Pd-Mediated Intramolecular C–H Activation

The precise role of base additives in promoting C–H activation has been the subject of several computational studies. Clot and Baudoin used B3PW91(DMF) calculations to study the reactions of 2-halo-*tert*-butylbenzene (**8**) at {$Pd(PR_3)$} species to form cyclobutarenes (**9**) (Figure 1.4a). These studies compared a model system (with R = Me) to those with the bulky phosphines used experimentally (R = ^{t}Bu [14, 15] or Cyp [16]). With R = Me and ^{t}Bu, the initial Ar–Br oxidative addition and subsequent C–H activation and C–C reductive elimination steps were all compared in the presence of three different bases (OAc, HCO_3^-, and CO_3^{2-}). Experimentally, use of CO_3^{2-} proved most efficient. Calculations on the PMe_3 model failed to capture this preference for carbonate and, moreover,

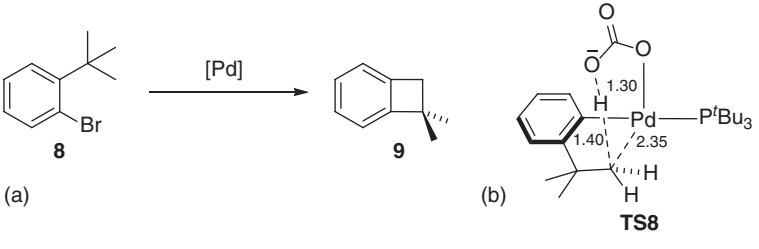

Figure 1.4 (a) Pd-catalyzed formation of cyclobutarenes and (b) transition state for C(sp^3)–H activation via deprotonation of a C–H bond that is geminal to an agostic interaction; key distances in Å [14].

did not identify C–H activation as the rate-limiting step as suggested by a significant experimental k_H/k_D kinetic isotope effect (KIE). In contrast, with the $\{Pd(P^tBu_3)\}/CO_3^{2-}$ model, a novel variation on the C–H activation mechanism was characterized whereby the bulk of the P^tBu_3 ligand promotes an isomer with carbonate *trans* to the agostic C–H of the substrate (Figure 1.4). From this position, the deprotonation of a geminal C–H bond can be accessed via **TS8** and is promoted by the greater acidity of this position due to the neighboring agostic interaction [17]. With this mechanism, C–H activation is more accessible with CO_3^{2-} than with acetate or bicarbonate, and this C–H activation also becomes rate limiting.

The role of the base was also considered by Rousseaux and coworkers in a joint experimental and computational study on $Pd(Ar)(Br)(PMe_3)_2$ (**10**, Ar = 2-(dimethylcarbamoyl)phenyl), a model for the $Pd(Ar)(OPiv)(PCy_3)_2$ (OPiv = pivalate, $^tBuCO_2^-$) used experimentally (see Figure 1.5) [18]. Efficient catalysis required both pivalate and carbonate additives, and B3LYP(toluene) calculations suggest that the carboxylate base is important not only for the C–H activation but also in promoting phosphine loss from the Pd center (**10** → **11**, $\Delta G = -0.6$ kcal mol^{-1}). C–H activation is computed to be strongly endergonic, and so the initial HOAc adduct formed, **12**, should rapidly revert back to **11**. This is avoided by the intervention of the carbonate additive which performs a rapid deprotonation, thus allowing the reaction to proceed to products. Kinetic studies show a zeroth-order dependence in [substrate], first order in [Pd], and saturation kinetics at [OPiv]:[Pd] > 3 : 1. The weak coordinating ability of the carbamoyl moiety is also important, as more basic amine substrates will displace one arm of the κ^2-OAc ligand in **11** to form a stable bidentate adduct from which C–H activation is much less accessible.

Additional factors, including the role of specific solvation and of some commonly used additives, have been included in the computational modeling of

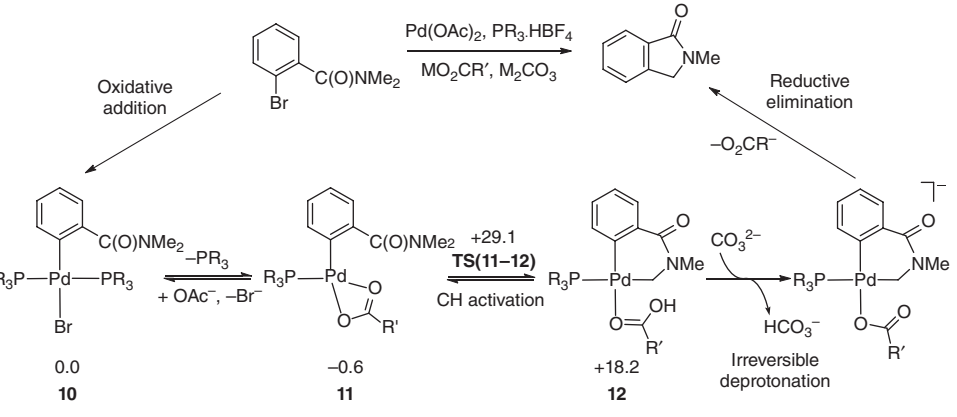

Figure 1.5 Pd-catalyzed formation of indolinones (experiment, R = Cy, R′ = ^{t}Bu) with selected key intermediates based on B3LYP calculations (R = Me, R′ = Me, relative free energies in kcal mol^{-1}) [18].

intramolecular C–H activation. Martínez and coworkers considered the role of the acidic medium in the cyclometalation of *N*-methylbenzylimine at $Pd(OAc)_2$ in acetic acid [19]. A dicationic intermediate, $[Pd(HOAc)_3(MeN{=}CHPh)]^{2+}$, was invoked to account for the rate acceleration observed in detailed kinetic studies performed in acidic media. B3LYP(MeOH) calculations (where MeOH was used to provide a dielectric similar to acetic acid) suggest C–H activation proceeds as a two-step process, the first involving displacement of an acetic acid ligand by the approaching *ortho*-C–H bond. The liberated acetic acid molecule then performs the deprotonation of the resultant agostic intermediate and leaves as an H_2OAc^+ cation (see **TS13**, Figure 1.6a). The overall barrier for this process is only 25 kJ mol^{-1}, with the deprotonation via **TS13** corresponding to the highest point on the profile.

The intervention of methanol solvent has also been considered in the C(sp^2)–H functionalization of *N*-methoxybenzamide at $Pd(OAc)_2$. M06(MeOH)//B3LYP calculations suggest that after *N*-deprotonation C–H activation proceeds with a computed barrier of 19.6 kcal mol^{-1}. However, a related transition state featuring an intervening MeOH molecule as a proton shuttle is competitive, at +22.4 kcal mol^{-1} (see **TS14**, Figure 1.6b) [20]. A similar role for external bicarbonate as a proton shuttle has been suggested by Wang, Wang, and coworkers for C–H activation of an anionic alanine amide species at Pd^{2+} (M06-L(DCE)//BP86; see **TS15**, Figure 1.6c) [21].

Supporting ligands can also play the role of the heteroatom base in C–H activation, as seen for an *N*-acyl monoprotected amino acid (MPAA) ligand studied by Houk, Yu, Wu, and coworkers (M06(SMD)//B3LYP calculations; see Figure 1.7a) [22]. This study also highlighted the flexibility of the directing group paradigm, with a remote cyano moiety providing access to an unusual *meta* selectivity in the reaction of substrate **16** with ethyl acrylate to give **17**. A combination of mass spectrometry and calculations provided evidence for a monomeric active species and, of several C–H activation mechanisms tested computationally, that proceeding via **TS16** in which the pendant *N*-acyl protecting group effects the deprotonation was most accessible ($\Delta G^{\ddagger} = 23.6$ kcal mol^{-1}). This is also consistent with the experimentally observed *meta* selectivity with barriers for activation

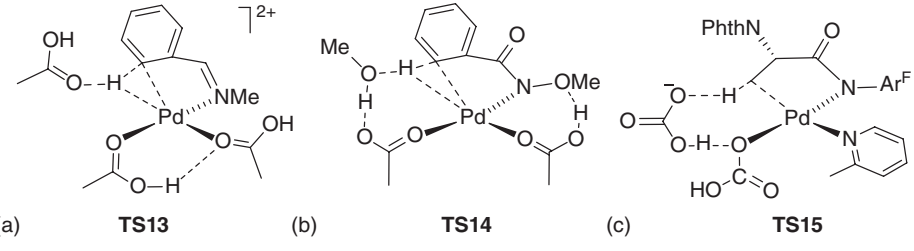

Figure 1.6 Cyclometalation transition state structures for (a) *N*-methylbenzylimine at $Pd(OAc)_2$ in acetic acid [19]; (b) *N*-methoxybenzamide at $Pd(OAc)_2$ in methanol [20]; and (c) an anionic alanine amide species at Pd(2-Me–C_5H_4N)(HCO_3) (PhthN = phthalimido; Ar^F = 4-C_6F_4–CF_3) [21].

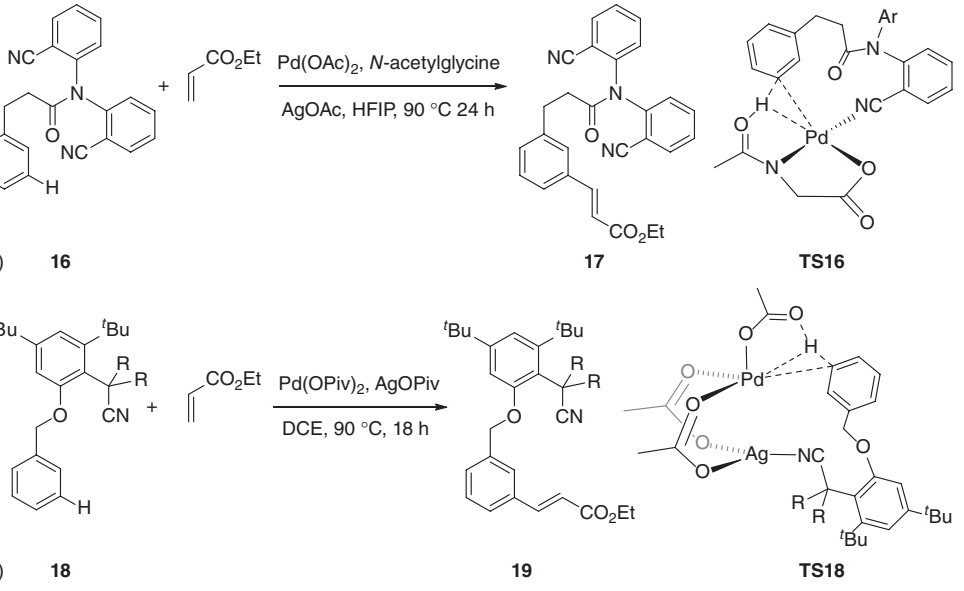

Figure 1.7 *Meta* selectivity via remote CN directing groups: (a) Pd-catalyzed alkenylation of **16**–**17** in the presence of an MPAA coligand via computed C–H activation transition state **TS16** featuring deprotonation by the *N*-acyl group (Ar = 2-C_6H_4–CN) [22] and (b) Pd/Ag-catalyzed alkenylation of **18**–**19** via computed heterobimetallic C–H activation transition state **TS18** [23].

at the *ortho* and *para* positions being slightly higher, by 0.9 and 0.5 kcal mol^{-1}, respectively. In a related study, the *meta*-selective C–H activation of **18** by a $Pd(OAc)_2$/AgOAc catalytic system was probed with M06(DCE)//B3LYP calculations (Figure 1.7b) [23]. A heterobimetallic $PdAg(OAc)_3$ system proved most compatible with experimental observations, with the remote CN group binding to Ag and directing the {Pd(OAc)} moiety to a *meta*-C–H bond (**TS18**). A computed barrier of 24.8 kcal mol^{-1} compares with barriers of 27.8 and 28.3 kcal mol^{-1} for *ortho*- and *para*-C–H activation, respectively. Other forms for the active species were considered but had higher computed barriers for *meta*-C–H activation ($Pd(OAc)_2$, 36.0 kcal mol^{-1}; $Pd_2(OAc)_4$, 29.3 kcal mol^{-1}; $Pd_3(OAc)_6$, 37.9 kcal mol^{-1}); moreover, for the monomeric and trimeric systems, an *ortho* selectivity was predicted.

Sunoj, Schaefer, and Anand have also considered the role of AgOAc and CsF additives in the $Pd(OAc)_2$-catalyzed amination of *N*-arylbenzamides with *N*-oxy- and *N*-chloromorpholines [24] (**20**–**21**, Figure 1.8) [25]. Using M06(DCE) calculations, a standard acetate-assisted C–H activation of the *N*-deprotonated substrate has a computed barrier of +28.1 kcal mol^{-1}. C–H activation at a range of monomeric as well as homo- and heterobimetallic species was then defined in which both additives were included. CsF is suggested to promote the initial *N*-deprotonation by forming HF; moreover, interaction of the Cs^+ cation with

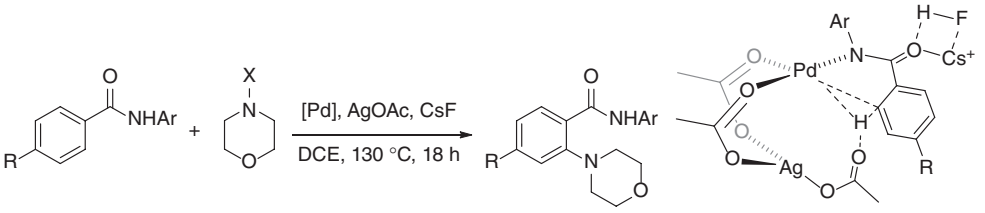

(a) **20** **21** (b) **TS20**

Figure 1.8 (a) Pd-catalyzed amination of N-arylbenzamides (experiment, R = ^{t}Bu, Ar = 4-$C_6F_4CF_3$, X = Cl, OAc,OBz) and (b) computed CsF-stabilized heterobimetallic transition state (R = Ar = H) [25].

both the acetate and HF can lead to significant stabilization in the subsequent C–H activation. The lowest-energy transition state was heterobimetallic **TS20**, which was computed to be 2.6 kcal mol^{-1} more stable than the isolated reactants. In all cases, the key elements of an AMLA/CMD C–H activation remain intact, that is, interaction with the Pd^{2+} metal center and efficient deprotonation by a nearby carboxylate ligand. Experimentally, the direct amination reaction requires heating to 130 °C for 18 h for efficient catalysis, and so the low barriers to C–H activation appear out of step with this. Presumably, the rate-determining step lies elsewhere in this catalytic cycle (e.g., the N–X activation or C–N coupling steps). In addition, the speciation of the "CsF" and "AgOAc" additives is particularly challenging. In this case, these are formulated as the solvent adducts $CsF(DCE)_6$ and $AgOAc(DCE)_2$, respectively. Such explicit solvation appears to be absent in the computed transition states, however.

A similar role for CsF in promoting *N*-deprotonation of amino acids at $Pd(Ph)(I)(PCy_3)$ has been proposed by Musaev, Yu, and coworkers using M06-L(toluene) calculations [26]. A second equivalent of "a molecule" of CsF is then implicated in the subsequent C(sp^3)–H activation where F^- plays the role of an external base to effect the C–H activation. These steps are part of a computed pathway for the direct arylation of amino acids in which the largest barrier is around 10 kcal mol^{-1}. This reaction requires heating to 100 °C, suggesting a disconnect between the computed pathway and the semiquantitative energetics implied by experiment. As above, the speciation of an ionic solid such as CsF in an aromatic solvent is especially challenging.

1.2.1.3 Intramolecular C–H Activation of Heterocyclic Substrates

Martínez, Urriolabeitia, and coworkers have studied the regioselective C–H activation of (Z)-2-aryl-4-arylidene-5(4*H*)-oxazolones, **22**, at $Pd(OAc)_2$ in acidic media [27]. As seen in related studies on *N*-methylbenzylimine [19], reactivity is enhanced by increased acidity and favors the arylidene position (i.e., C–H^a) to give, unusually, a six-membered palladacycle, isolated as a dimer. B3LYP($MeCO_2H$) calculations (X = Y = H) showed reduced barriers to C–H activation upon sequential protonation of the Pd active species and

that the dicationic intermediate, $[Pd(MeCO_2H)_3(\kappa\text{-}N\text{-}\mathbf{22})]^{2+}$, provided the best agreement with experimental activation data. A two-step C–H activation process was characterized involving initial displacement of one acetic acid ligand and formation of an agostic intermediate followed by deprotonation by the external acetic acid (similar to **TS13**, Figure 1.6). The kinetic preference for C–H^a bond activation reflects a lower degree of reorganization involved in this process. Barriers were further reduced when computed with the analogous CF_3CO_2H system, consistent with enhanced reactivity seen experimentally. The nature of these two-step C–H activations does vary, however, with the higher transition state corresponding to C–H bond cleavage in $MeCO_2H$ but changing to the formation of the agostic intermediate in F_3CCO_2H.

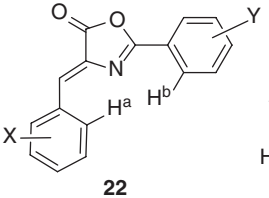

22

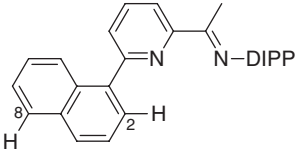

23

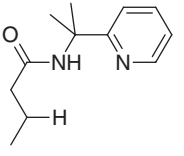

24

Regioselective formation of six-membered palladacycles was also observed with naphthyl moieties fitted with a bidentate *N,N*-pyridylarylimine directing group (**23**, DIPP = 2,6-$C_6H_3{}^iPr_2$). BP86-D3(toluene) calculations on the full experimental system defined a two-step C–H activation process that is favored at the C8-position both kinetically ($\Delta\Delta G^{\ddagger} = 1.8$ kcal mol^{-1}) and thermodynamically ($\Delta\Delta G = 3.5$ kcal mol^{-1}) over a one-step process at the C2-position [28]. With monodentate 2-naphthylpyridine, both the kinetic and thermodynamic preference swaps to the 2-position, consistent with experimental observations and indicating that the additional imine anchor is indeed responsible for the change in selectivity. $Pd(OAc)_2$-mediated C(sp^3)–H bond activation of alkylamides fitted with a removable 2-pyridylisopropyl directing group (**24**) has been characterized with a barrier of 23.6 kcal mol^{-1} with M06-2X//B3LYP calculations [29].

Houk, Yu, and coworkers have investigated stereoselective C(sp^3)–H activation as part of the Pd(II)-catalyzed iodination and acetoxylation of oxazoline derivatives **25** (see Figure 1.9) [30]. M06//B3LYP calculations indicated the nature of the resting state to be crucial in controlling reactivity. With a bulky substrate ($R^1 = R^2 = {}^t$Bu, **25a**), this is the $Pd_3(OAc)_6$ trimer and C–H activation has an overall barrier of 26.2 kcal mol^{-1}. In contrast, when R^1 = Et and $R^2 = {}^i$Pr (**25b**), a rather stable monomer, $Pd(OAc)_2(\kappa\text{-}N\text{-}\mathbf{25b})_2$, is formed from which C–H

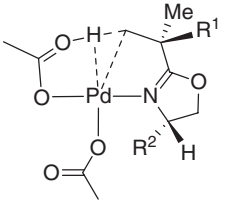

Figure 1.9 Computed C–H activation transition state for C(sp^3)–H bond activation of oxazolines ($R^1 = R^2 = {}^t$Bu, **25a**; R^1 = Et, $R^2 = {}^i$Pr, **25b**), highlighting the preferred *anti* arrangement for **25a** [30].

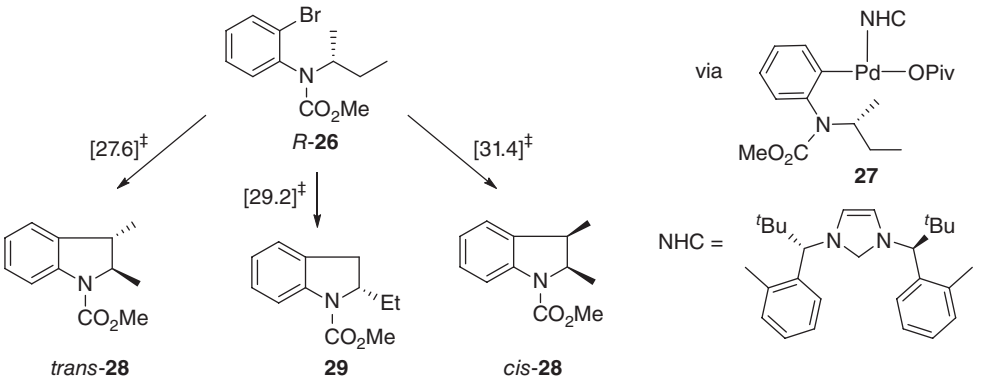

Figure 1.10 Enantioselective indoline formation from *R*-**26** via Pd–NHC intermediate **27.** Free energies (at 413 K) for the enantio-determining C–H activation transition states leading to products *cis*-/*trans*-**28** and **29** are indicated in kcal mol^{-1} [31a].

activation entails a barrier of 38.4 kcal mol^{-1}. The highly stereoselective reaction with **25a** is traced to a preferred *anti* arrangement of the bulky ^{t}Bu substituents in the transition state, this being 2.3 kcal mol^{-1} more stable than alternative *syn* forms. This $\Delta\Delta G^{\ddagger}$ equates to a 96% diastereomeric excess, de (cf. 82% experimentally), while with **25b** $\Delta\Delta G^{\ddagger} = 0.8$ kcal mol^{-1}, giving a calculated de of 17% (cf. 0% experimentally).

Further evidence of the ability of DFT calculations to capture the subtle energetics associated with enantioselective processes was seen in an M06-L(xylenes) study of the asymmetric synthesis of indolines reported by Kündig and coworkers (see Figure 1.10) [31]. For example, with indoline *R*-**26**, Ar–Br activation at the Pd(NHC) catalyst followed by Br/OPiv substitution accesses intermediate **27**. From here C–H activation favors the methylene position and specifically the C–H bond that gives rise to the *trans* isomer of the product (*trans*-**28**). C–H activation of the methyl group (leading to **29**) is then preferred to activation of the methylene C–H bond leading to *cis*-**28**. Computed free energy barriers with *S*-**26** and a benzyl analog also match the experiment product distributions. The origin of the enantioselectivity is traced to destabilizing interactions with the NHC ligand, and similar results were obtained with the B97-D functional.

1.2.2
Intermolecular C–H Activation

1.2.2.1 Early Computational Studies

The first computational study of heteroatom-assisted intermolecular C–H activation was reported in 2000 by Sakaki and coworkers, who studied the C–H activation of benzene and methane at $M(O_2CH)_2$ (M = Pd, Pt) at the MP4(SDQ) level [32]. For benzene, this involved a two-step process with $\kappa^2 - \kappa^1$ displacement

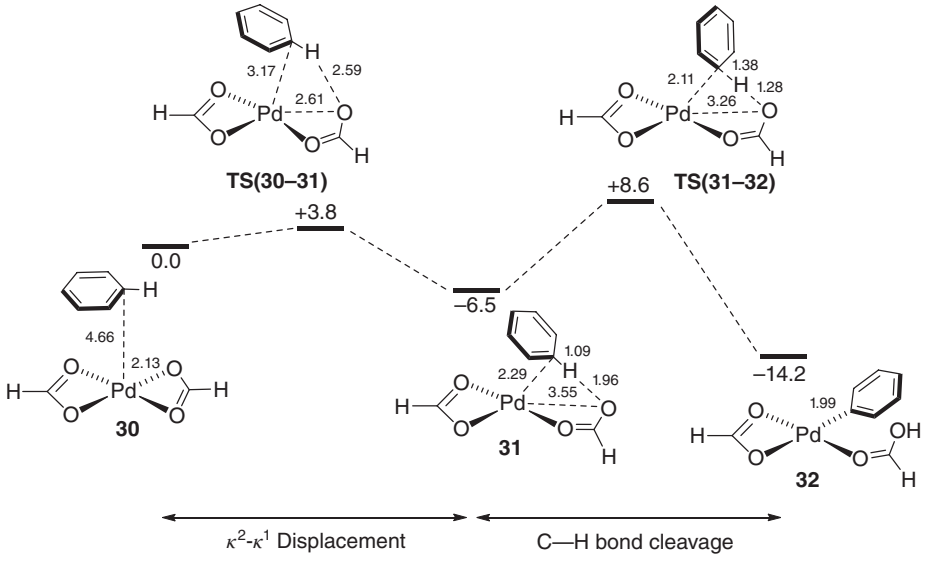

Figure 1.11 Computed reaction profile for C–H activation of benzene at Pd(κ^2-$CO_2H)_2$; MP4(SDQ) energies are in kcal mol^{-1} and selected distances in Å [32].

of one formate ligand to give an intermediate σ-complex (**31**, Figure 1.11), which features a short H · · · O contact of 1.96 Å (Figure 1.11). This facilitates the subsequent heterolytic cleavage of the C–H bond.

The observation that fluorinated arenes are particularly effective substrates in the $Pd(OAc)_2$-catalyzed direct arylation of aryl halides prompted Fagnou and coworkers to consider the mechanism of C–H activation [33]. Using B3LYP calculations, several mechanisms were considered at a Pd(Ph)(X)(PH_3) model species (X = Br, HCO_3), and a concerted metalation with proton abstraction by the intramolecular bicarbonate base found to be most accessible (see Figure 1.12 where **TS33** was computed with the full P^{t}Bu$_2$Me ligand). The absence of any Pd · · · F interactions indicated a truly nondirected C–H activation process. Moreover, no pathway relating to a S_EAr process could be located, and this, along with the greater reactivity associated with the more acidic C–H bonds of fluoroarenes, suggested a different mechanistic interpretation was required for such processes. The term "concerted metalation deprotonation," was later

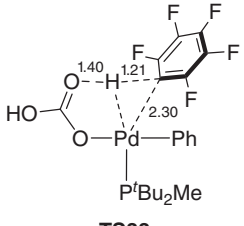

Figure 1.12 Computed transition state for C–H bond activation of C_6F_5H at Pd(Ph)(HCO_3)(P^{t}Bu$_2$Me), with selected distances in Å [33].

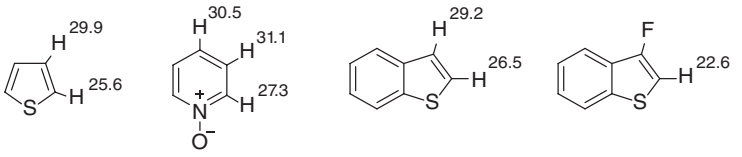

Figure 1.13 Computed free energy activation barriers (kcal mol^{-1}) for C–H activation of selected heterocycles at Pd(Ph)(OAc)(PMe_3) [35].

adopted by this group. A follow-on study showed a slightly reduced computed barrier with OPiv as the base (24.9 kcal mol^{-1}) compared to OAc (26.2 kcal mol^{-1}) [34].

The CMD concept was generalized in a 2008 B3LYP study by Gorelsky, Lapointe, and Fagnou that considered a wide range of (hetero)aromatic substrates. In particular, electron-rich arenes, hitherto thought to react via S_EAr processes, were shown instead to react via the CMD mechanism [35]. Moreover, the CMD pathway correctly reproduces the observed regioselectivities, including preferential reaction at the 2-position of thiophene and the *ortho* position of pyridine *N*-oxide (Figure 1.13). The accelerating effect of electron-withdrawing substituents is again apparent, for example, in the lower barrier for C2–H activation of 3-fluorobenzothiophene compared to benzothiophene. The overall trends in reactivity and the regioselectivities predicted in this paper were subsequently verified experimentally [36].

This and subsequent papers by Gorelsky [37] employed the activation strain model [38] to analyze trends in the CMD activation barriers (see Figure 1.14 for C–H activation of benzene). In this approach, the activation energy, ΔE_{act}, for C–H activation at Pd(Ph)(OAc)(PMe_3) is decomposed into two terms, ΔE_{dist}, the sum of the energies required to distort the individual reaction components to

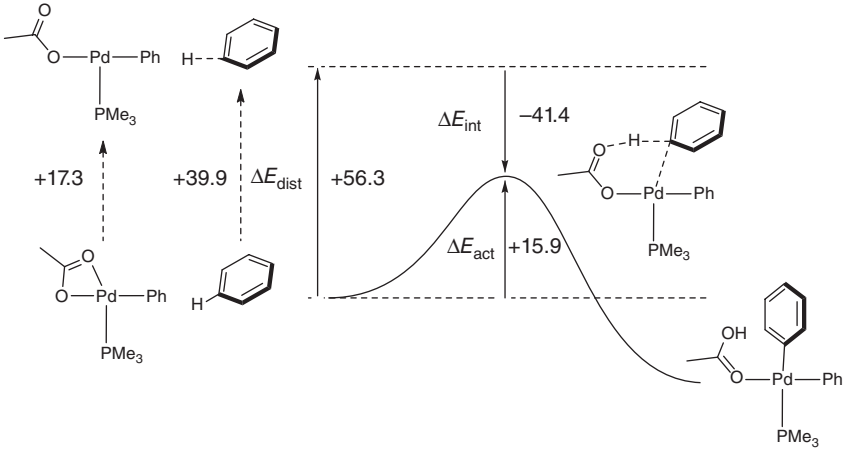

Figure 1.14 The activation strain model illustrated for C–H activation of benzene at Pd(Ph)(κ^2-OAc)(PMe_3) with component energies indicated in kcal mol^{-1} [37a].

their geometries seen in the transition state, and ΔE_{int}, the energy of interaction between these two fragments. This permitted a wide range of substrates to be categorized into one of three classes, depending on which was the dominant contribution to the overall barrier. For Class I substrates, ΔE_{dist} dominates, and in particular the distortion associated with the substrate C–H bond; this destabilizing terms tends to be lower with more acidic C–H bonds, such as in C_6F_5H and other electron-deficient substrates such as heterocyclic *N*-oxides. For Class II species, ΔE_{int} dominates, and this stabilizing term is enhanced by more nucleophilic substrates. Finally, for Class III substrates, variations in both ΔE_{dist} and ΔE_{int} must be considered. Computed reaction profiles indicate the possibility of precomplexation of the substrate at Pd, as either π-bound, heteroatom-bound, or C–H-bound adducts. In no case was a Wheland intermediate located and with the very electron-deficient C_6F_5H no precursor was seen. Gorelsky has summarized this body of work in a recent review, including an overview of C–H activation in heterocyclic *N*-oxides, azoles, thiophenes, and F- and Cl-substituted arenes [37b].

The direct arylation of polyfluorinated arenes, Ar^F–H, has also been considered by Eisenstein, Perutz, and coworkers [39]. Starting from a Pd(Ph)(κ^1-OAc)(DMA)(PMe_3) adduct (DMA = dimethylacetamide), B3PW91(DMA) calculations provided energetics for DMA/arene substitution, C–H activation, loss of AcOH, and the final C–C coupling and loss of the biaryl product. The computed trends were found to depend on the number of *ortho*-F substituents present. DMA/arene substitution is always endergonic but is most accessible with substrates with no *ortho*-F for which η^2-CH=CH adducts are located. With two *ortho*-F weak Pd · · · C–H adducts are seen, where this interaction is supported by H bonding to the pendant arm of the κ^1-OAc ligand. Two *ortho*-F substituents also promote the C–H activation step such that this group of substrates has the lowest overall barriers to CH activation. After loss of HOAc, C–C reductive coupling was then found to be disfavored by *ortho*-F substituents. The trends in C–H activation are shown to correlate well with both C–H bond acidities (as judged by computed heterolytic bond dissociation energies) and the homolytic bond strength of the new Pd–Ar bond in the Pd(Ar^F)(Ph)(κ^1-OAc)(PMe_3) intermediates. This latter factor also serves to increase barriers for C–C coupling. Overall, the C–H activation step is more sensitive to the F substituents as the effects of both the C–H acidity and the Pd–Ar^F bond strengths reinforce each other; in contrast, for the C–C coupling, the need to break a stronger Pd–Ar^F bond is counteracted by the formation of a stronger Ph–Ar^F bond. Ess and coworkers have also emphasized the role of the Pd–Ar bond strength on the regioselectivities of (hetero)arene activation at Pd(Ph)(κ^2-OAc)(PMe_3) (M06 calculations) [40]. Gorelsky has since questioned this in his recent review [37b] and reemphasized the role of the ΔE_{int} term, noting the lack of relationship between this and the computed Pd–Ar^F heterolytic dissociation energies. However, as the Pd–Ar^F bond strength is only one component of the ΔE_{int} term, these two interpretations are not necessarily contradictory.

1.2.2.2 Direct Functionalization via C–H Activation of Heterocyclic Substrates

Synthetic protocols are now in place for a range of direct functionalizations with heterocyclic substrates, and the field is still expanding rapidly. This activity is matched by parallel computational studies, where in many cases the full catalytic cycle is considered. In the following, the discussion will focus on the computational understanding of the C–H activation step, but the importance of this step within the context of the overall catalytic cycle will also be discussed, where appropriate.

Gorelsky and Lapointe modeled C–H activation at the 5-position of 2-substituted thiophenes at a Pd(Ph)(κ^2-OAc)(PMe_3) model system, with computed barriers (B3LYP) referenced against the parent unsubstituted thiophene [37a]. A correlation with the substrate's nucleophilic character as gauged by Hammett σ_p parameters was found, and a correlation between σ_p and both ΔE_{act} and ΔE_{dist} was also seen. Lower barriers were computed with both electron-withdrawing substituents (CN, CO_2Me) and certain electron-donating groups (*N*-pyrrolidine), and these implied higher reactivities were corroborated by experimental competition studies. That both electron-withdrawing and electron-donating groups can be more reactive reflects the counterbalancing effects of enhanced acidity (less favorable ΔE_{int}, more favorable ΔE_{dist}) versus enhanced nucleophilicity (more favorable ΔE_{int}, less favorable ΔE_{dist}). The relationship between σ_p and the components of the activation strain model is significant: negative gradient Hammett plots are often taken to be indicative of S_EAr character, but this study shows they can also be compatible with heteroatom-assisted C–H activation processes. Further B3LYP calculations confirmed that introduction of an electron-withdrawing chloro substituent into substituted thiophenes or *N*-methylindoles not only enhances reactivity but can also induce useful regioselectivities in the subsequent C–H functionalization steps [41]. This is synthetically attractive as the Cl substituent can both be readily and regioselectively introduced and then (after C–H functionalization) easily removed by conventional means.

The role of different *para*-substituted triarylphosphines, P(4-$C_6H_4R)_3$ (R = H, OMe, F, and CF_3), in controlling trends in the direct arylation of thiazole and 2-methylthiophene substrates has been investigated by Ozawa and coworkers using M06-2X(THF)//B3LYP calculations [42]. Experimentally, the rate of reaction at Pd(Ar)(κ^2-OAc){P(4-$C_6H_4R)_3$} intermediates (Ar = 2,6-$C_6H_3Me_2$) follows opposite trends for thiazole (R = CF_3 > F > H > OMe) and 2-methylthiophene (R = OMe > H > F > CF_3). Calculations (Ar = Ph, Figure 1.15) trace this to a change in the rate-determining steps between these two systems. With thiazole, C–H activation via **TS34** is rate limiting, and the barrier for this process reflects variation in the energies of the *N*-bound precursors that are stabilized by more electron-withdrawing phosphines. In contrast, with 2-methylthiophene, C–C reductive coupling is rate limiting (**TS35**), and this process is promoted by electron-donating phosphines.

The unusual C4-selective arylation of 2,3-disubstituted thiophenes reported by Itami and coworkers [43] has been the subject of two theoretical studies.

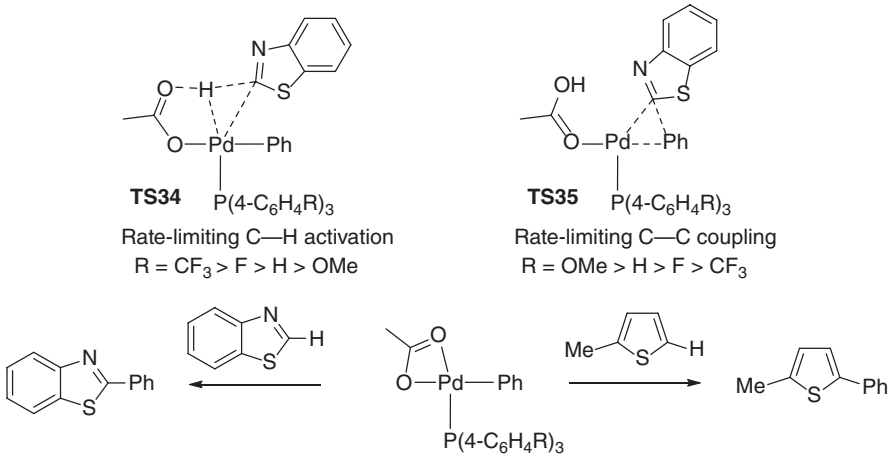

Figure 1.15 Different reactivity trends in the direct arylation of thiazole and 2-methylthiophene [42].

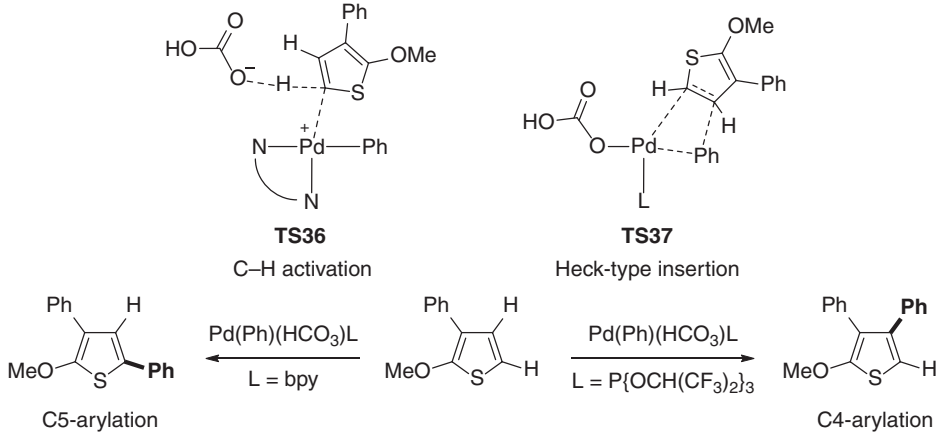

Figure 1.16 C4 versus C5 selectivity in the direct arylation of 2-phenyl-3-methoxythiophene [45].

Experimentally, the regioselectivity is controlled by the choice of coligand, with 2,2′-bipyridine (bpy) giving C5-arylation and $P\{OCH(CF_3)_2\}_3$ giving C4-arylation. Grimme, Itami, Studer, and coworkers used dispersion-corrected DFT (B2PLYP-D3//TPSS-D3) to model the reaction of $[Pd(bpy)Ph]^+$ with the parent thiophene and showed that insertion into the Pd–Ph bond had an intrinsic preference for phenyl transfer onto the C4-position [44]. Fu and coworkers considered the reactions of 2-phenyl-3-methoxythiophene at $Pd(Ph)(\kappa^1\text{-}CO_3H)(bpy)$ and $Pd(Ph)(\kappa^2\text{-}CO_3H)\{P(OR)_3\}$ (R = OMe, $CH(CF_3)_2$) using an M06(toluene)//B3LYP protocol [45]. In the bpy system, C–H activation at C5 proceeds with a computed barrier of 29.9 kcal mol^{-1} via **TS36** (see Figure 1.16). The bidentate nature of

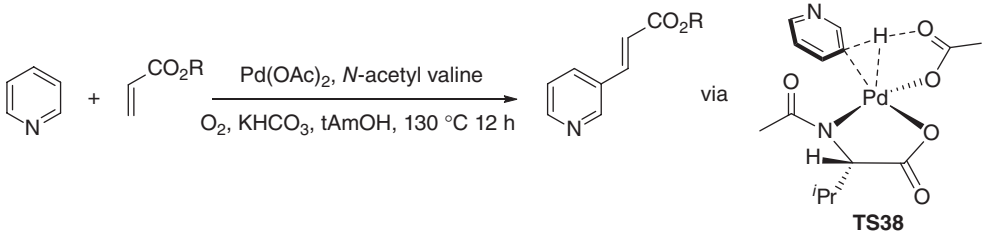

Figure 1.17 Pd-catalyzed *meta*-selective alkenylation of pyridine in the presence of an MPAA coligand (experiment R = ^{n}Bu; computed R = Et) [46].

the bpy ligand requires the initial displacement of the bicarbonate ligand by the incoming thiophene, with the bicarbonate then effecting an external deprotonation. The alternative Heck-type insertion of the thiophene favors Ph transfer onto the 4-position but has a slightly higher barrier of 31.6 kcal mol^{-1}. Initial calculations on a Pd(Ph)(κ^2-CO_3H){$P(OMe)_3$} model gave a similar outcome, and it was only by using the full P{$OCH(CF_3)_2$} ligand in the calculations that the swap in regioselectivity was reproduced, with barriers of 36.7 kcal mol^{-1} for C–H activation at C5 and 34.4 kcal mol^{-1} for insertion with Ph transfer to C4 via **TS37**. Experimentally, the reaction proceeds at 130 °C in 12 h. The authors postulate that specific H-bonding interactions in the transition state control the C4 regioselectivity and that this is only introduced once the full P{$OCH(CF_3)_2$} ligand is considered.

The *meta*-selective C–H activation of pyridine and other electron-deficient monosubstituted arenes has been modeled by Wu, Zeng, and coworkers using B3LYP(1-pentanol) calculations [46]. This step is part of a $Pd(OAc)_2$-catalyzed Heck alkenylation using MPAA coligands (see Figure 1.17). The calculations employed *N*-acetyl-valine which upon *N*-deprotonation and in the presence of pyridine forms Pd(κ^1-OAc)(NC_5H_5){κ-*N*,*O*-{AcONCH(^{i}Pr)CO_2}} as the precursor to C–H activation. Rearrangement from an *N*-bound to a π-bound pyridine adduct ($\Delta G = +17.1$ kcal mol^{-1}) precedes C–H activation, and for the *meta* position, this proceeds through a CMD transition state, **TS38**, with an overall barrier of 31.0 kcal mol^{-1}. This pathway proves slightly more accessible than either *ortho*-C–H activation ($\Delta G^{\ddagger} = 32.4$ kcal mol^{-1}) or *para*-C–H activation ($\Delta G^{\ddagger} = 31.9$ kcal mol^{-1}). Note that the potential noninnocence of the *N*-acetyl group in C–H activation has been subsequently highlighted (see Figure 1.7) [22]. Reprotonation then facilitates *N*-decoordination of the MPAA ligand, and this is thought to facilitate the functionalization steps (modeled with ethylacrylate). A related study by Zhang and coworkers considered monosubstituted arenes [47].

Gorelsky has modeled the C–H activation step in the direct arylation of both free and Cu(I)-bound azoles at a Pd(Ph)(κ^2-OAc)(PMe_3) intermediate [37c]. These two reactions provide complementary regioselectivities, with reaction at C5 favored for the free azoles but C2-arylation favored in the presence of Cu(I) salts. With *N*-methylimidazole and oxazole, the formation of *N*-bound

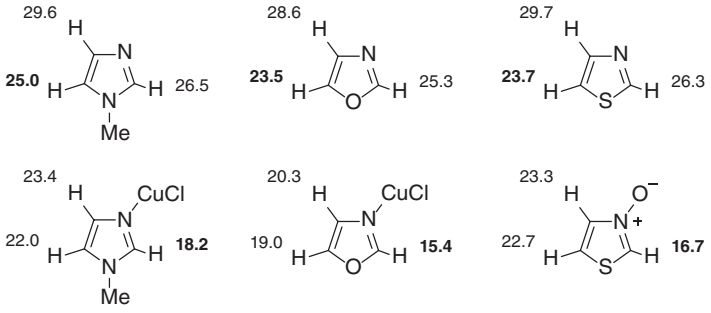

Figure 1.18 Computed free energy activation barriers (kcal mol^{-1}) for C–H activation at Pd(Ph)(κ^2-OAc)(PMe_3) for *N*-methylimidazole and oxazole (with and without bound CuCl), thiozole, and thiazole *N*-oxide [37c].

CuCl adducts leads to a significant lowering of the computed barriers to C2–H activation, consistent with the observed swap in regioselectivity (see Figure 1.18). The Lewis acidic CuCl additive switches the behavior of the azole from a Class II ligand (substrate nucleophilicity dominant) [48] to a Class I species (C–H bond acidity dominant). Formation of the thiazole *N*-oxide has a similar effect with the B3LYP-computed barrier for C2–H bond activation being 16.7, 9.6 kcal mol^{-1} lower than the free thiazole. Gorelsky and DeBoef also considered C–H activation of *N*-alkylindoles as a step in the direct C2-arylation of these species [49]. A CMD mechanism is again found to accommodate electronically diverse substituents in the C6-position with changes in computed barriers interpreted in terms of the Class II behavior of this substrate; regioselectivities were also correlated to changes in the distribution of the highest occupied molecular orbitals of these species.

Both Sakaki [50] and Sanford and Schoenebeck [51] have studied the Pd-mediated C–H oxidative coupling of benzo[h]quinoline with arenes. The latter study focused on changes in regioselectivity observed with 1,3-dimethoxybenzene (DMB), depending on whether acetate (*meta*/*meta*) or carbonate (*ortho*/*para*) is used. M06-L(DMSO/DMB)//ωB97X-D calculations on both monomeric and dimeric intermediates featuring a cyclometalated benzo[h]quinoline ligand suggest that C–H activation of 1,3-dimethoxybenzene proceeds through a CMD transition state with the same *ortho/para* selectivity irrespective of whether acetate or carbonate is used (the latter being modeled as "$NaCO_3^-$"). In contrast, the subsequent C–C coupling step (which is promoted by benzoquinone) proceeds with *meta/meta* selectivity, again for both bases. The observed swap in selectivity arises as a change in the base also changes the identity of the rate-determining step. With carbonate, this is the C–H activation, which leads to *ortho/para* selectivity. However, with acetate, the C–C reductive elimination transition state lies marginally above that for C–H activation, and so the *meta/meta* selectivity is favored.

The $Pd(OAc)_2$-catalyzed oxidative coupling of *N*-methylimidazole (as a model for xanthines) with thiophene has been modeled by Hu, You, and coworkers

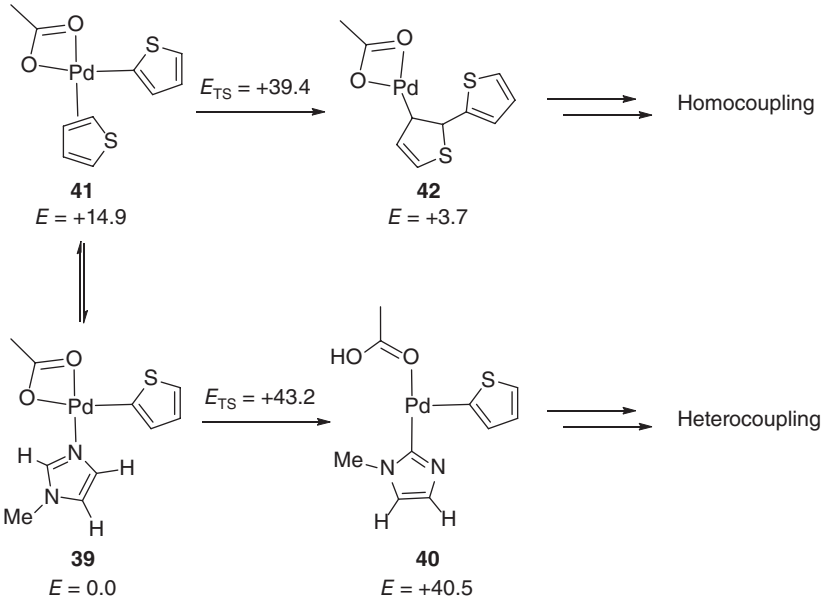

Figure 1.19 Computed key stationary points with energies in kcal mol^{-1} for the reactions of thiophene and *N*-methylimidazole at a $Pd(OAc)_2$ catalyst [52].

using B3LYP calculations [52]. $Pd(OAc)_2$ is considered to be the active species at which thiophene readily undergoes C–H activation at the 2-position with a barrier of only 9.6 kcal mol^{-1} (see Figure 1.19). This process is described as a S_EAr reaction, although the computed transition state appears similar to many CMD-like processes in the literature. Binding of *N*-methylimidazole then forms an intermediate, **39**, from which C–H activation at the 2-position of the *N*-methylimidazole proceeds with a barrier of 43.2 kcal mol^{-1} to give **40**. Alternatively, the substitution of *N*-methylimidazole by a second thiophene gives **41** from which a Heck-type insertion of the C2=C3 bond of this second thiophene into the extant Pd-thiophenyl bond has been characterized. This process has a slightly lower barrier of 39.4 kcal mol^{-1} relative to **39**, but would imply homocoupling via **42**, contrary to experimental observations. Further study of this discrepancy would be of interest. Experimentally, the reaction proceeds in 1,4-dioxane at 120 °C and requires 20 h. Shaik and Kosuch have also commented on the importance of concentration effects in controlling homo- versus heterocoupling in oxidative coupling reactions [53].

The speciation of the $Pd(OAc)_2$ catalyst in such reactions is a key point. For example, Hartwig and Tan have shown that the $Pd(OAc)_2$-catalyzed direct arylation of 2-bromotoluenes and benzene proceeds more efficiently in DMA solvent in the absence of added phosphine ligands [54]. A preformed dianionic dimer, $[ArPdBr_2]_2^{2-}$, was also active. B3LYP calculations showed that C–H activation of benzene at Pd(Ph)(κ^2-OPiv)(DMA) has a computed free energy barrier of 31 kcal mol^{-1} compared to a barrier of 42 kcal mol^{-1} at Pd(Ph)(κ^2-OPiv)(P^tBu_3).

It is postulated that steric hindrance around the Pd center disfavors reaction in the presence of bulky phosphines and that "ligandless" C–H activation may be accessible for these unactivated substrates.

The importance of heterocyclic *N*-oxides in synthesis has prompted computational and experimental mechanistic studies of their reactivity. Campeau and coworkers performed both kinetic studies and supporting B3LYP calculations on the direct arylation of pyridine *N*-oxide [55]. Under catalytic conditions, the coupling of *para*-nitropyridine *N*-oxide with 5-bromo-*m*-xylene was shown to be zeroth order in the aryl bromide, first order in the pyridine *N*-oxide, and half order in the Pd catalyst (whether supplied as either $Pd(OAc)_2$/$[P^tBu_3PH][PF_6]$ or $Pd(P^tBu_3)_2$). Zero-order kinetics in $[P^tBu_3]$ were also observed, and side-by-side experiments comparing pyridine *N*-oxide and pyridine *N*-oxide-d_5 revealed a k_H/k_D KIE of 3.3. These outcomes suggest a mechanism involving facile loss of P^tBu_3 and Ar–Br activation, followed by rate-determining C–H activation of the pyridine *N*-oxide, with the formation of a dimeric resting state between these two events. B3LYP calculations confirmed that C–H activation at the 2-position of pyridine *N*-oxide at $Pd(Ph)(\kappa^2\text{-}CO_2R)(PMe_3)$ proceeds through an inner-sphere CMD process with computed barriers of 34.9 kcal mol^{-1} (R = OH) and 34.1 kcal mol^{-1} (R = CH_3). The effects of a range of different substituents around the pyridine ring were also successfully rationalized computationally. Further stoichiometric reactions of *para*-nitropyridine *N*-oxide were also performed to assess the role of base, starting with a preformed $Pd(Ph)Br(P^tBu_3)$ reactant. In this case, use of K_2CO_3 alone gave very low yields, but 30% conversion was seen with KOPiv, either with or without K_2CO_3. Further runs showed that achieving the observed catalytic activities required excess K_2CO_3 but only a substoichiometric amount of KOPiv. Thus, K_2CO_3 is proposed to act as a terminal proton acceptor to avoid the buildup of pivalic acid in solution. This interpretation was supported by stoichiometric runs using $Pd(Ph)(\kappa^2\text{-}OAc)(P^tBu_3)$, **43**, which gave the same yield whether run with or without K_2CO_3. It was noticeable, however, that the product yield in these runs (about 48%) was lower than expected from the performance of the catalytic process.

Picking up on this point, Hartwig and coworkers revisited this system and showed that **43** is in fact inactive toward pyridine *N*-oxide [56]. Instead, a cyclometalated dimer, $[Pd(OAc)(^tBu_2PCMe_2CH_2)]_2$ (**44**, formed via decomposition of **43**), was proposed to be the active species. Kinetic studies showed direct arylation at **44** to be first order in pyridine *N*-oxide and half order in the dimer. These results indicate opening of dimer **44** to give the cyclometalated monomer, $Pd(\kappa^2\text{-}OAc)(^tBu_2PCMe_2CH_2)$, **45**, which then effects the C–H activation. The inactivity of the monomeric bromo-analog, $Pd(Br)(^tBu_2PCMe_2CH_2)$, suggested that C–H activation proceeds via a CMD pathway involving acetate rather than the cyclometalated arm of the phosphine ligand. Further runs in the presence of both **43** and **44** showed a zeroth-order dependence on [**43**], confirming its non-involvement in the C–H activation. Finally, B3LYP calculations demonstrated a reduced C–H activation barrier of 27 kcal mol^{-1} at **45** compared to 33 kcal mol^{-1} at **43**. Based on these results, a cooperative mechanism shown in Figure 1.20

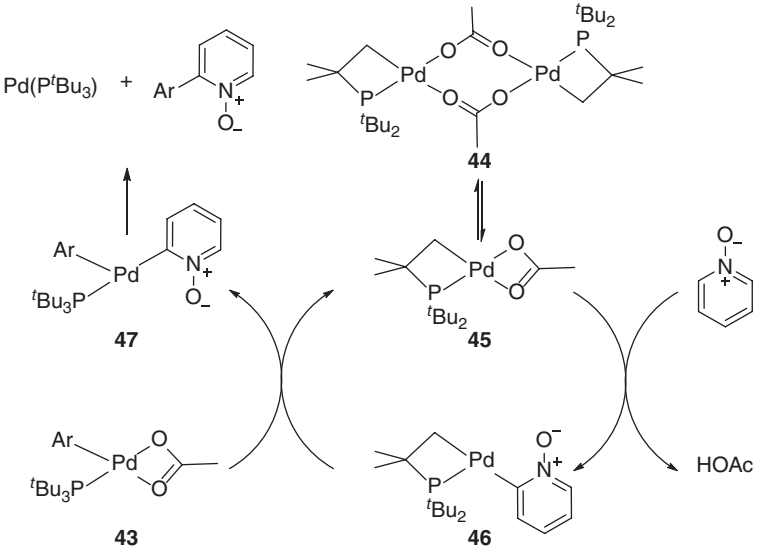

Figure 1.20 Proposed mechanism for the direct arylation of pyridine *N*-oxides in the $Pd(OAc)_2/P^tBu_3$ system. Figure adapted from reference [56].

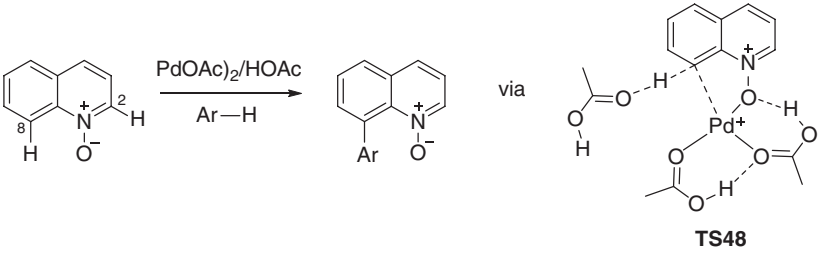

Figure 1.21 Direct, C8-selective arylation of QNO by $Pd(OAc)_2$ in acetic acid and the proposed computed transition state [57].

was proposed. In this, the pyridine *N*-oxide undergoes C–H activation at **45** to generate a heteroaryl ligand in **46**. This then undergoes exchange with the OAc ligand in **43** to regenerate **45** and form $Pd(Ar)(Ar')(P^tBu_3)$, **47**. Reductive elimination from **47** releases the biaryl product and $Pd(P^tBu_3)$, with the latter reforming **44**/**45** under the catalytic conditions.

Larionov and coworkers have described the $Pd(OAc)_2$-catalyzed direct arylation of quinolone *N*-oxides (QNOs) in acetic acid, a process that proceeds selectively at the 8-position (Figure 1.21) [57]. B3LYP(HOAc) calculations suggest this process occurs at dicationic $[Pd(HOAc)_3(\kappa\text{-}O\text{–QNO})]^{2+}$, with C–H activation involving an agostic intermediate formed via displacement of one HOAc molecule that then acts as an external base. This is a similar scenario to that described by Martíniz, Urriolabeitia, and coworkers [27]. A barrier of

24.7 kcal mol^{-1} is computed via a five-membered transition state, **TS48**; in comparison, activation at the 2-position involves a four-membered transition state and hence a much higher barrier of 40.4 kcal mol^{-1}. C–H activation is also endergonic, consistent with the observation of H/D exchange experimentally. Comparison with the equivalent reactions at a Pd(Ph)(κ^2-OAc)(PMe_3) model intermediate shows C–H activation at the C2-position would be favored ($\Delta G^{\ddagger} = 29$ kcal mol^{-1}).

1.3 Ruthenium, Rhodium, and Iridium

Much of the insight gained from computational and mechanistic studies into heteroatom-assisted C–H activation at Pd(II) metal centers has proven to be applicable to Ru(II), Rh(III), and Ir(III) systems. Therefore, only a brief overview of the most relevant computational studies of these processes will be presented. Computational studies of Ru-, Rh-, and Ir-catalyzed C–H functionalization reactions will then be described. Most of these target the synthesis or derivatization of heterocycle systems and also include a treatment of the initial C–H activation step.

1.3.1 Intramolecular Heteroatom-Assisted C–H Activation

In 2006, Davies, Macgregor, and coworkers investigated the cyclometalation of Me_2NCH_2Ph by $[IrCl_2Cp^*]_2$ in the presence of NaOAc [58]. Acetate plays a dual role in this process, by both inducing dimer opening and acting as a base in the subsequent C–H activation. Initial BP86 calculations on a model $[Ir(Me_2NCH_2Ph)(\kappa^2\text{-OAc})Cp]^+$ system characterized a concerted C–H activation incorporating dissociation of one Ir–O bond and deprotonation by the pendant acetate arm (i.e., an AMLA-6 process). This process was favored over either deprotonation by the Ir-bound oxygen (AMLA-4) or an oxidative addition to an Ir(V)-hydride. Later [58b], a slightly lower-energy two-step pathway featuring an agostic intermediate was characterized, with rate-limiting $\kappa^2 - \kappa^1$ displacement of acetate at +13.4 kcal mol^{-1}. Lower barriers were computed with weaker bases, RCO_2^- (R = Me > Ph > HO > CCl_3 > CF_3), reflecting the fact that a weak base will also be a poor ligand and so facilitate the rate-limiting $\kappa^2 - \kappa^1$ carboxylate displacement step. The cyclometalation of *N*-methyl-2-pyrrole imine was also considered [59].

Maseras, Dixneuf, and coworkers subsequently studied the cyclometalation of 2-phenylpyridine at the $[RuCl_2(p\text{-cymene})]_2$ dimer in the presence of *N*-heterocyclic carbene ligands [60]. B3LYP calculations were performed using a *cis*-$RuCl_2$(IMe)(2-Ph–C_5H_4N) model system (where IMe = 1,3-dimethylimidazol-2-ylidene) with bicarbonate base. Although this species showed a distinct agostic interaction *trans* to the IMe ligand, a concerted

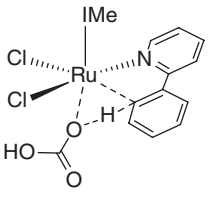

TS49

Figure 1.22 C–H activation transition state for cyclometalation of 2-phenylpyridine at {*cis*-Ru(Cl)$_2$(IMe)} in the presence of bicarbonate base [60].

oxidative addition to a Ru(IV)-hydride proved very unfavorable. Instead, coordination of bicarbonate is preferred from which a low-energy intramolecular deprotonation can be accessed with a barrier of only 13.9 kcal mol^{-1} via **TS49** (Figure 1.22). This involves the Ru-bound oxygen atom and a four-membered (i.e., AMLA-4) transition state.

More recently, Davies, Macgregor, and coworkers highlighted the importance of dispersion effects when seeking a more quantitative assessment of observed data [61]. Experimentally, *N*-alkylimines (**H-L$_{1-5}$**) and 2-phenylpyridine (**H-L$_6$**) react at [MCl$_2$Cp*]$_2$/NaOAc (M = Rh, Ir) to give well-defined cyclometalated species as their chloride adducts (Figure 1.23a). Moreover, H/D exchange experiments indicate irreversible C–H activation at Ir (kinetic control) but reversible C–H activation at Rh (thermodynamic control). Competition experiments also gave different trends in the reactivity of these species at each metal.

These features were studied with BP86-D3 calculations, in either MeOH (Rh) or CH_2Cl_2 (Ir) solvent. Computed profiles for the reactions of the 2-thiophenyl derivative **H-L$_3$** are shown in Figure 1.24. OAc-induced opening of the [MCl$_2$Cp*]$_2$ dimer followed by substitution of one anionic ligand by **H-L$_3$** forms **IV$_M$**. For Rh, a two-step C–H activation is characterized via an agostic intermediate, **V$_{Rh}$**, to give the cyclometalated HOAc adduct **VI$_{Rh}$**. Cl/HOAc substitution leads to the observed product **VII$_{Rh}$**. The energetics of this process ($\Delta G_{calc} = -4.0$ kcal mol^{-1}; $\Delta G^{\ddagger}_{calc} = 11.8$ kcal mol^{-1}) indicate reversible C–H activation, consistent with the observed H/D exchange. For Ir, the reaction is both more exergonic ($\Delta G_{calc} = -14.2$ kcal mol^{-1}) and has a much higher barrier ($\Delta G^{\ddagger}_{calc} = 18.4$ kcal mol^{-1}), consistent with an irreversible reaction under kinetic control. Moreover, C–H activation proceeds in a single step, corresponding to $\kappa^2-\kappa^1$ displacement of OAc. Experimentally, the Rh system is less efficient and takes much longer to achieve reasonable yields. The lower barrier for Rh indicates this is not a kinetic effect but rather reflects a slow approach to equilibrium that ultimately favors product formation.

Importantly, use of both an extended basis set (with diffuse functions) and the D3 correction proved essential to reproduce the favorable thermodynamics expected for all metal/substrate combinations. This reflects the stabilization derived from having the bulky substrate adjacent to the {MCp*} fragment and in turn stresses the importance of using the full experimental system in the calculations. With this approach, the more subtle trends in the relative reactivity of the six substrates were also reasonably captured. Thus, for Rh (Figure 1.23a, thermodynamic control), the trend in ΔG_{calc} largely follows the increase in

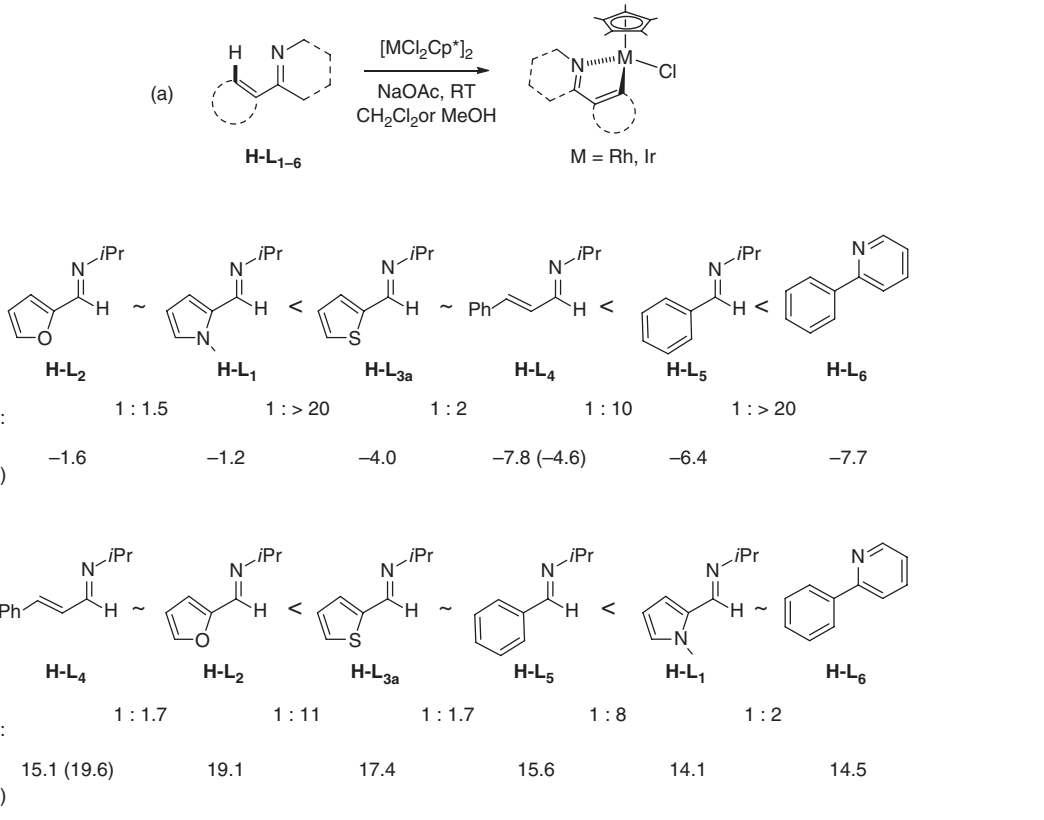

Figure 1.23 (a) Cyclometalation of *N*-alkylimines (**H-L$_{1-5}$**) and 2-phenylpyridine (**H-L$_6$**) at $[MCl_2Cp^*]_2$ (M = Rh, Ir); relative experimental and computed reactivities for substrates **H-L$_{1-6}$** at $[MCl_2Cp^*]_2$, (b) M = Rh, and (c) M = Ir. Computed data (kcal mol^{-1}) give the overall free energy changes, ΔG_{calc}, for M = Rh and calculated activation barriers, $\Delta G^{\ddagger}_{calc}$, for M = Ir [61].

substrate reactivity, whereas for Ir (Figure 1.23b, kinetic control), increased substrate reactivity is mirrored in a decrease in $\Delta G^{\ddagger}_{calc}$. One exception was **H-L$_4$**, the reactivity of which was overestimated for both metals. This is thought to relate to the different shape of this substrate (which features a vinyl CH=CHPh substituent rather than the aromatic substituents in **H-L$_{1-3}$** and **H-L$_5$**) and the propensity of the dispersion correction to emphasize intramolecular stabilization over interaction with the environment (e.g., solvent). A different degree of dispersion stabilization therefore occurs upon binding **H-L$_4$** to the metal fragment. To explore this issue, a model substrate **H-L$_4$′** featuring a smaller CH=CH$_2$ substituent was computed (values in parenthesis in Figure 1.23), and this gave both a reduced ΔG_{calc} at Rh and an increased $\Delta G^{\ddagger}_{calc}$ at Ir.

Around the same time, Zheng and coworkers [62] modeled the acetate-assisted cyclometalation of *N*-phenylbenzaldimines at $[MCl_2Cp^*]_2$ dimers (M = Rh, Ir). B3LYP(MeOH) calculations found cyclometalation at Ir to be favored

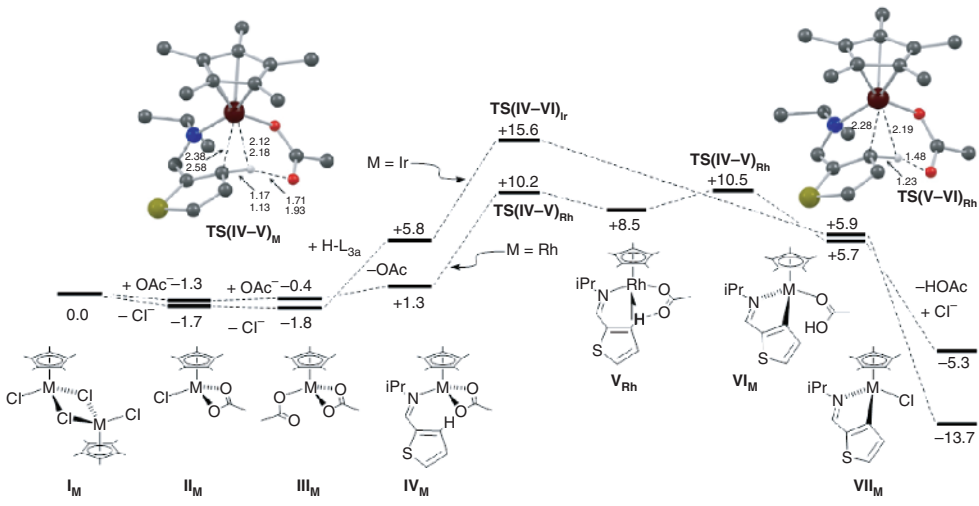

Figure 1.24 Computed free energy reaction profiles (kcal mol^{-1}) for C–H activation of **H-L$_3$** at [MCl$_2$Cp*]$_2$ for M = Ir (in CH_2Cl_2) and M = Rh (in MeOH). Computed C–H activation transition states are shown with key distances in Å (Rh, plain text; Ir, *italics*) and nonparticipating H atoms omitted for clarity.

thermodynamically (Rh, $\Delta G_{calc} = -0.5$ kcal mol^{-1}; Ir, $\Delta G_{calc} = -8.4$ kcal mol^{-1}), but, contrary to the above study, the C–H activation barrier was higher for Rh (Rh, $\Delta G^{\ddagger}_{calc} = 26.4$ kcal mol^{-1}; Ir, $\Delta G^{\ddagger}_{calc} = 19.7$ kcal mol^{-1}). Experimentally, the reaction is slower with Rh [63]. The effect of phenyl substituents, R, positioned *meta* to the directing group, was also assessed. When R = CF_3 or Me, C–H activation is computed to be kinetically favored at the less hindered *ortho*-C–H bond, as seen experimentally. With R = OMe, the two pathways are computed to be in competition, while for R = F, activation of the adjacent *ortho*-C–H bond is favored (perhaps reflecting the "*ortho*-effect" of fluorine [64]). Experimentally, a mixture of products is seen when R = OMe and F.

1.3.2 Intermolecular C–H Activation

Extensive computational work has been published on the intermolecular C–H bond activation of benzene at Ru(II), Rh(III), and Ir(III) metal centers fitted with a heteroatomic base as a ligand. When this base is a κ^2-carboxylate ligand, the C–H mechanism has been shown to be similar to analogous reactions at Pd(II) carboxylates. Computational studies of benzene C–H activation have been reported at Ir(κ^2-CO_3)Cp(PMe_3) [37a], [Ir(κ^2-OAc)Cp(PMe_3)]$^+$[65], and Ir(acac)$_2$(κ^2-OAc) (acac = acetylacetonoate) [66]. García-Melchor, Gorelsky, and Woo also compared the C–H activations of benzene, 2-methoxythiophene, 2,3-dimethylfuran, and *N*-methylindoles at a [Ir(Ph)(κ^2-CO_3)(PMe_3)(py)] catalyst and found reactivity trends were accommodated within a CMD-type mechanism [67].

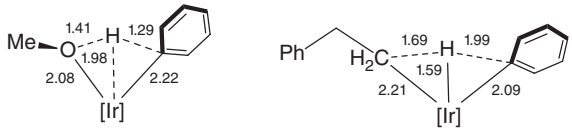

TS50 **TS51**

Figure 1.25 Comparison of OMe-assisted and σ-bond metathesis transition states at [Ir]R species ([Ir] = $Ir(acac)_2$; R = OMe, **TS50** [68]; R = $PhCH_2CH_2$, **TS51** [69]). Key selected distances are given in Å.

In addition to processes involving a bidentate base, C–H activation can also be facilitated by a monodentate ligand, X (X = OR, NR_2), acting as a heteroatomic base. This results in a net 1,2-addition of the C–H bond over the M–X single bond via a four-membered transition state. Two key computational studies characterized this process. Firstly, Oxgaard, Goddard, and coworkers studied the C–H activation of benzene at $Ir(acac)_2(OMe)$ using B3LYP calculations [68]. Orbital analysis of the computed pathway via **TS50** (Figure 1.25) highlighted the role of the oxygen lone pair in promoting a proton transfer. This contrasts with a related σ-bond metathesis process (**TS51**) [69], where a pair of electrons in an M–C bond is used to accept the transferring proton. These authors categorized the heteroatom-assisted process as an "internal electrophilic substitution" (IES).

Shortly afterward, Gunnoe, Cundari, and coworkers reported B3LYP calculations on benzene C–H activation at a series of isoelectronic d^6 $[(Tab)M(X)(PH_3)]^q$ model species (Tab = tris(azo)borate; X = OH, OPh, or NHPh and including M = Ru ($q = 0$) and Ir ($q = 1$)) [70]. Analysis of the four-membered transition state using the atoms-in-molecules approach revealed an absence of a bond critical point between the transferring hydrogen and the metal center. This is again distinct from σ-bond metathesis in related Ir(III) systems where a direct Ir–H interaction is seen. The availability of a lone pair of the heteroatomic base, X, is again the key feature, leading the authors to characterize this process as in intramolecular deprotonation. The interaction of the electron-deficient metal center also renders the C–H bond more acidic and so facilitates deprotonation.

Ess, Periana, Goddard, and coworkers subsequently compared four-membered and six-membered C–H activation transition states in a B3LYP study on the C–H activation of benzene at $Ir(acac)_2(X)$ species (X = OH, OAc) [66]. An activation strain model was used to compare the performance of hydroxide and acetate, where the latter could access both four-membered and six-membered transition states, depending on whether the proton transfers onto the Ir-bound or pendant oxygen, respectively. C–H activation via a six-membered process is favored and is associated with a lower ΔE_{dist} term compared to the more constrained four-membered transition states. The acetate and hydroxide four-membered transition states are very similar.

More recently, further computational studies of the C–H activation of benzene at Ir [71] and Rh [72] have appeared, while Jones and coworkers compared aryl $C(sp^2)$–H bond activation and alkyl $C(sp^3)$–H bond activation

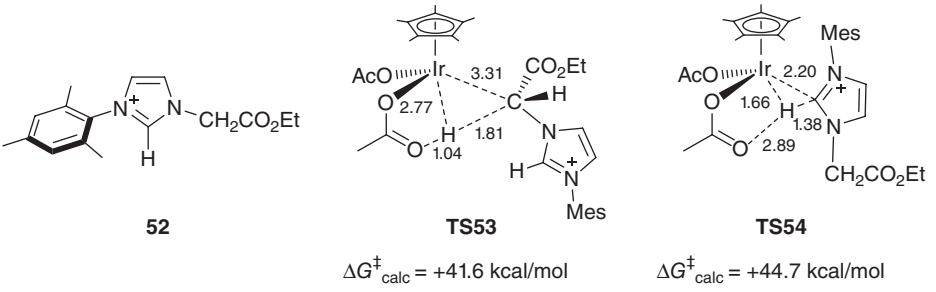

52 **TS53** **TS54**

$\Delta G^{\ddagger}_{calc}$ = +41.6 kcal/mol $\Delta G^{\ddagger}_{calc}$ = +44.7 kcal/mol

Figure 1.26 Key distances (Å) and relative free energies (kcal mol^{-1}) in transition states for C(sp^3)–H activation (**TS54**) and C(sp^2)–H activation (**TS55**) of an α-imidazolium ester, **53**, at Ir(OAc)$_2$Cp*.

of isopropylbenzene at [M(bdmpza)Cl$_3$]$^-$ complexes (M = Rh, Ir; bdmpza = *bis*-(3,5-dimethylpyrazol-1-yl)acetate; B3LYP(TFA)) [73]. Competing C(sp^2)–H and C(sp^3)–H bond activation processes of α-pyridinium and α-imidazolium esters (Figure 1.26, **52**) at [IrCl$_2$Cp*]$_2$/NaOAc were reported by Cross and coworkers. M06(CH$_2$Cl$_2$)//B3LYP calculations showed the observed C(sp^3)–H activation to be kinetically favored over the thermodynamically preferred C(sp^2)–H activation [74]. Both processes involve a nondirected C–H activation and initiate from H-bonded adducts formed at Ir(κ^1-OAc)$_2$Cp*. Although the computed barriers of >40 kcal mol^{-1} are rather high for room temperature processes, the different transition state geometries show some interesting features: C(sp^3)–H activation is dominated by interaction with the base (**TS53**: C···H = 1.81 Å, O···H = 1.04 Å, Ir···H = 2.77 Å), while the metal plays a more prominent role in the C(sp^2)–H activation (**TS54**: C···H = 1.38 Å, O···H = 2.89 Å, Ir···H = 1.66 Å). This is consistent with the AMLA concept in which the complementary involvement of base and metal combines to accommodate the activation of a wide range of different C–H bonds [59].

1.3.3
C–H Activation and Functionalization

A range of studies have now appeared modeling complete catalytic cycles based on an initial C–H bond activation and the subsequent functionalization steps. The functionalization processes involve reactions with an insertion partner (an alkyne, an alkene, or a carbene/nitrene source) and lead to the formation of new heterocyclic rings or direct replacement of the C–H bond with a new C–R group. In many cases, the focus of the computational studies is on these functionalization processes as well as the reoxidation steps (particularly with internal oxidants). The C–H activation in these catalytic processes is typically of the intramolecular AMLA-6 type, although exceptions do exist, as will be detailed later. Input from parallel experimental studies, including the determination of k_H/k_D KIEs, the observation of H/D exchange, competition experiments, and the isolation of key intermediates both complement and provide benchmark data

for the computational modeling. In the following, figures will show the model systems used in the calculations and relevant experimental results and conditions will be given in the text.

1.3.3.1 Heterocycle Formation with Internal Oxidants

In 2011, Guimond and coworkers published the first computational study of Rh(III)-catalyzed heterocycle formation based on initial C–H activation and subsequent functionalization [75]. The coupling of benzamides with alkynes to give isoquinolones was considered, with an OR group (OR = OMe, OPiv) installed on the benzamide nitrogen to act as an internal oxidant. B3LYP(MeOH) calculations were performed for the model reaction of *N*-acetoxybenzamide with acetylene at a model $Rh(OAc)_2Cp$ catalyst (see Figure 1.27). After *N*-deprotonation and loss of HOAc, directed *C*–H activation proceeds with an overall barrier of

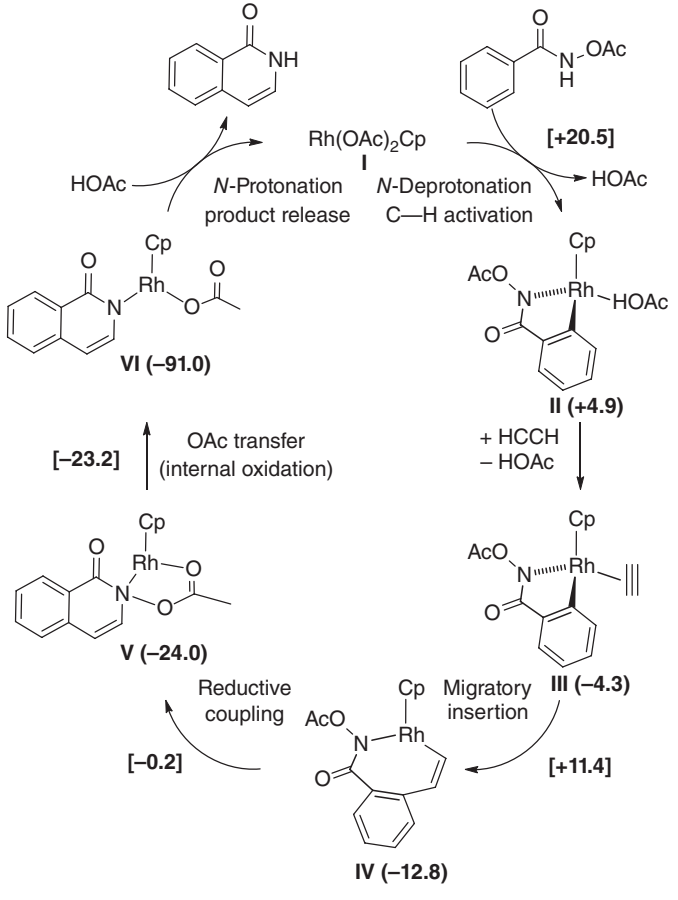

Figure 1.27 Computed catalytic cycle for the coupling of *N*-acetoxybenzamide with acetylene at $Rh(OAc)_2Cp$ [75]. Computed free energies of intermediates and transition states are given in kcal mol^{-1}, with the latter indicated in square brackets, and are quoted relative to the reactants at 0.0 kcal mol^{-1}.

20.5 kcal mol^{-1}. The alternative C–H activation of the neutral (i.e., *N*-protonated) substrate was considerably less accessible. Facile HOAc/HCCH substitution, insertion, and N(sp^3)–C(sp^2) reductive coupling then led to intermediate **V** in which the isoquinolone is bound to Rh (Rh–N = 2.13 Å) and the *N*-acetate group bridges the Rh–N bond (N–O = 1.49 Å; Rh–O = 2.21 Å). N–O bond cleavage with transfer of acetate then occurs with a minimal barrier of 0.8 kcal mol^{-1} with concomitant formal Rh(I) to Rh(III) oxidation. Protonolysis by HOAc then releases the isoquinolone product and completes the catalytic cycle. The calculations suggest rate-limiting C–H activation, consistent with the observation of a large k_H/k_D KIE when an *N*-(pivaloyloxy)benzamide substrate was used experimentally. However, as no KIE is observed with *N*-methoxybenzamide, the nature of the rate-limiting step is clearly substrate dependent.

An important complement to this study was published by Xia and coworkers in 2012 who considered the mechanism of 3,4-dihydroquinolone formation via the coupling of alkenes with PhC(O)NH(OR), where the OR group dictates whether N(sp^3)–C(sp^3) coupling (OR = OPiv) or β-H elimination occurs (OR = OMe; see Figure 1.28a for the case of ethene) [76]. M06(MeOH) calculations compared profiles for the reactions of both benzamides with ethene at a Rh(OAc)$_2$Cp* catalyst. Very similar N–H and C–H activation profiles are computed in each case, with overall barriers of about 18 kcal mol^{-1} and the endergonic formation of the HOAc adducts ($\Delta G_{calc} \approx +4$ kcal mol^{-1}) indicating reversible C–H activation. After HOAc/ethene substitution, insertion forms a conformationally flexible seven-membered rhodacycle ($\mathbf{I_{OR}}$, Figure 1.28b) from which a low-energy isomer can be accessed when OR = OPiv ($\mathbf{I'_{OR}}$, Figure 1.28c) which features an interaction between the pendant oxygen and the metal center.

From these seven-membered rhodacycles, the mechanisms diverge. For OR = OMe (Figure 1.28b), facile β-H transfer followed by formal N–H reductive coupling produces the Rh(I) intermediate $\mathbf{III_{OMe}}$. Reaction with HOAc then facilitates the cleavage of the N–O bond ($\Delta G^{\ddagger}_{calc} = 13.6$ kcal mol^{-1}), forming MeOH and the Rh(III) species $\mathbf{IV_{OMe}}$. A transition state for reoxidation via OMe transfer onto Rh in $\mathbf{III_{OMe}}$ is 22.4 kcal mol^{-1} higher in energy. A second HOAc then protonates the amide nitrogen in $\mathbf{IV_{OMe}}$, releasing the product and regenerating the catalyst. A transition state for alternative direct C–N coupling from $\mathbf{I_{OMe}}$ was located, but at +43.8 kcal mol^{-1} it is too high to be competitive. In contrast, N–O bond cleavage in $\mathbf{I'_{OPiv}}$ (Figure 1.28c) with transfer of the OPiv group onto Rh ($\Delta G^{\ddagger}_{calc} = 14.3$ kcal mol^{-1}) is now favored over β-H transfer and N–H reductive coupling ($\Delta G^{\ddagger}_{calc} = 23.2$ kcal mol^{-1}, $\mathbf{I_{OR}}$ to $\mathbf{III_{OPiv}}$, Figure 1.28b). The OPiv group is thought to play several roles in this mechanistic swap: the extra Rh–O interaction in the seven-membered rhodacycle $\mathbf{I'_{OPiv}}$ disfavors the initial β-H transfer step, while the greater bulk of the OPiv unit also destabilizes the alkene intermediate, $\mathbf{II_{OPiv}}$, making β-H transfer endergonic. The Rh–O interaction in $\mathbf{I'_{OPiv}}$ also facilitates N–O bond cleavage and affects the internal oxidation to give a Rh(V) nitrene intermediate ($\mathbf{V_{OPiv}}$, Rh–N = 1.871 Å). This species then undergoes facile C–N reductive coupling and protonolysis to complete the cycle.

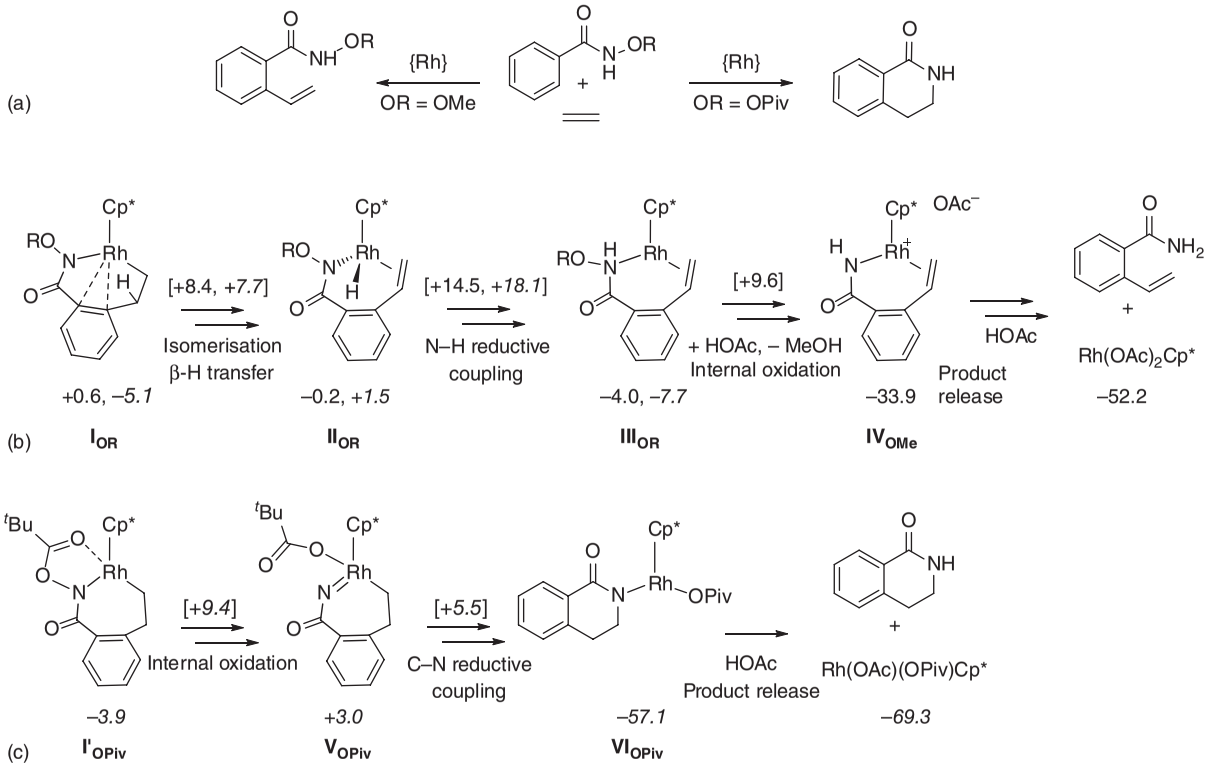

Figure 1.28 (a) Reactions of PhC(O)NH(OR) (OR = OMe, OPiv) with ethene at $Rh(OAc)_2Cp^*$ [76]. Key stationary points (kcal mol^{-1}; free energies quoted relative to the reactants at 0.0 kcal mol^{-1}) for (b) alkenylation for OR = OMe and OPiv (in italics); data for the onward reaction of $\mathbf{III}_{OR}$ for OMe only; and (c) C(sp^3)–N coupling for OR = OPiv. Double arrows indicate several steps are involved with the energy of the highest transition state between the two minima indicated in square brackets.

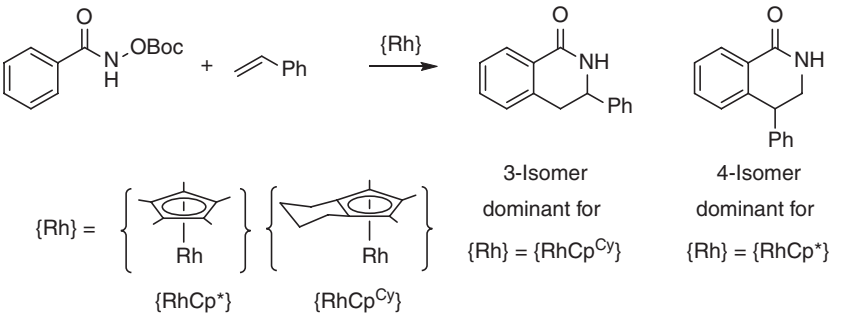

Figure 1.29 Regioselective dihydroisoquinolone formation with Rh-cyclopentadienyl catalysts [77].

The regioselectivity of dihydroisoquinoline formation between PhC(O)NHOBoc (OBoc=OC(O)^{t}Bu) and styrene has been studied with ωB97X-D(MeOH) calculations (Figure 1.29) [77]. Experimentally, {RhCp*} catalysts favor the 4-isomer and {RhCp^{Cy}} catalysts favor the 3-isomer. Calculations based on the pathway defined by Xia above indicate very similar transition state energies for the insertion and internal oxidation steps. This made quantitative predictions about selectivity difficult, and so the computed data were used as a basis for kinetic simulations. These predicted a 76 : 24 ratio in favor of the 3-isomer with {RhCp^{Cy}}, in excellent agreement with experiment. For {RhCp*}, the computed ratio is 49 : 51, indicating that the 4-isomer does become relatively more favored, although this is underestimated compared to experiment where a 16 : 84 ratio is seen. The authors point out that a 0.5 kcal mol^{-1} shift in energy would reproduce this result, highlighting the challenge to theory when attempting to model such subtle selectivity effects.

Ma and coworkers have considered the related coupling of *N*-acetoxybenzamide with allene-enes to construct eight-membered lactam rings (Figure 1.30) [78]. Using a Rh(CO_3)Cp* catalyst, M06(MeOH) calculations suggest that the carbonate can effect both the *N*-deprotonation and (as HCO_3^-) the subsequent C–H activation. The C–H activation barrier of 20.8 kcal mol^{-1} is the highest along the computed profile, consistent with efficient catalysis at room temperature and a significant k_H/k_D KIE. C–H activation was computed to be endergonic ($\Delta G_{calc} = +5.4$ kcal mol^{-1}), although experimentally no H/D exchange was seen in the absence of the coupling partner. Coordination of the allene-ene permits insertion of first the distal allenic double bond and then the terminal alkene to form seven- and then nine-membered rhodacyclic intermediates (**55** and **56**, respectively). The profile proceeds as in Figure 1.28c, with the key OAc transfer to give a Rh(V) nitrene again shown to be favored over β-H transfer/N–H reductive coupling. A related study by Huang and Chen on the Rh($OAc)_2$Cp*-catalyzed coupling of PhC(O)NHOR (OR = OPiv, OMe) with both cyclohexylallene and 1,1-dimethylallene was recently reported [79]. M06(MeOH)//B3LYP calculations confirm the observed regioselectivities: with cyclohexylallene, the 4-isomer

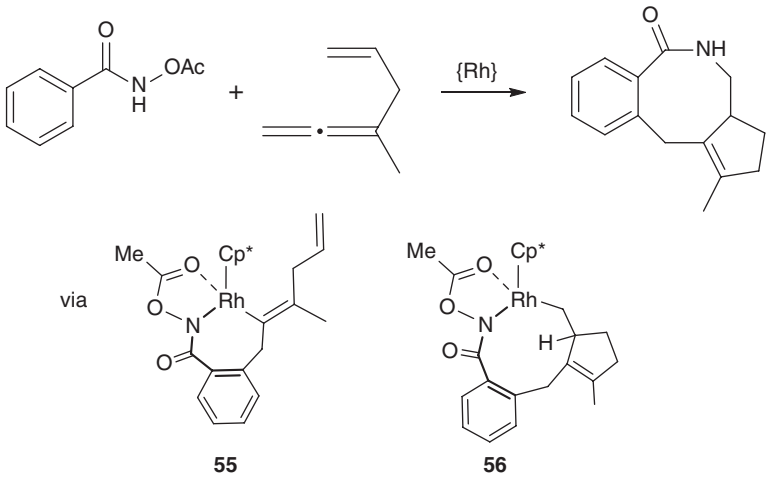

Figure 1.30 Rh-catalyzed lactam formation from *N*-acetoxybenzamide and 3-methylhexa-1,2,5-triene [78].

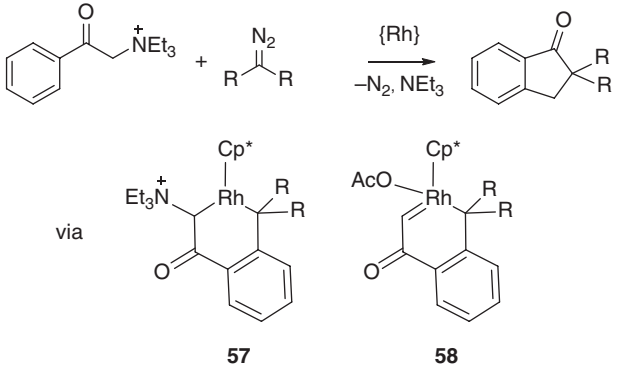

Figure 1.31 Rh-catalyzed benzocyclopentanone formation from benzophenone ammonium salts and α-diazoesters (R = $CO_2{}^i$Pr) [80].

(cf. Figure 1.30) is favored, but with 1,1-dimethylallene, greater steric hindrance in the insertion transition state drives the formation of the 3-isomer.

Ammonium groups can also act as internal oxidants, with C–N bond cleavage resulting in loss of an amine and formation of carbocyclic products. Lan, Wan, Li, and coworkers used M06(MeCN) and B3LYP-D3(MeCN) calculations to model $Rh(OAc)_2Cp^*$-catalyzed benzocyclopentanone formation from benzophenone ammonium salts and α-diazoesters (Figure 1.31) [80]. Initial deprotonation and loss of HOAc forms an enolate intermediate from which C–H activation proceeds preferentially from the C-bound form ($\Delta G^{\ddagger}_{calc}$: M06 = 27.2 kcal mol^{-1}, B3LYP-D3 = 26.3 kcal mol^{-1}); barriers via the O-bound isomer were 2–3 kcal mol^{-1} higher. The subsequent steps involve diazoester coordination and N_2 loss

followed by carbene insertion to give **57**. NEt_3 loss and coordination of OAc then gives **58** via a transition state at 25.2 kcal mol^{-1} (M06) or 20.7 kcal mol^{-1} (B3LYP-D3). **58** is a Rh(V) carbene complex that is isoelectronic with the previous Rh(V) nitrene species. Carbene insertion and protonolysis then complete the cycle. Overall, the initial C–H activation is rate limiting, consistent with an observed k_H/k_D KIE of about 4. C–H activation is, however, computed to be endergonic, which implies a reversibility not seen in attempted H/D exchange reactions. The authors postulate that this discrepancy may be due to the presence of CsOAc in the catalytic system that slows the reverse protonolysis.

N–N bond cleavage as a means of internal oxidation has been exploited in the coupling of 2-acetyl-1-arylhydrazines with alkynes to give indoles (Figure 1.32). This $Rh(OAc)_2Cp^*$-catalyzed reaction was studied by Chen and Lin who reported M06(DCE) energetics with an additional D3 correction [81]. After deprotonation, the terminal NAc position acts as a directing group for a two-step C–H activation via $\mathbf{I_{NAc}}$. Unusually, C–H bond cleavage from the agostic intermediate has a significant additional barrier of 10.5 kcal mol^{-1}, giving an overall barrier for C–H activation of 25.9 kcal mol^{-1}. HOAc/PhCCPh substitution gives $\mathbf{II_{NAc}}$, from which alkyne insertion (via a transition state at 29.2 kcal mol^{-1}) gives $\mathbf{III_{NAc}}$ at −5.1 kcal mol^{-1}. This isomerizes first via a facile 1,2-Rh shift to $\mathbf{IV_{NAc}}$ and then by an HOAc-assisted H^+ transfer to $\mathbf{V_{NAc}}$. C–N reductive coupling constructs the indole moiety ($\mathbf{VI_{NAc}}$) which is bound to a formally Rh(I) center and an NHC(O)Me group. The latter then transfers onto Rh to generate a Rh(III) species ($\mathbf{VII_{NAc}}$). Reaction with HOAc induces loss of H_2NOAc, protonolysis of the Rh–N bond, and release of the indole.

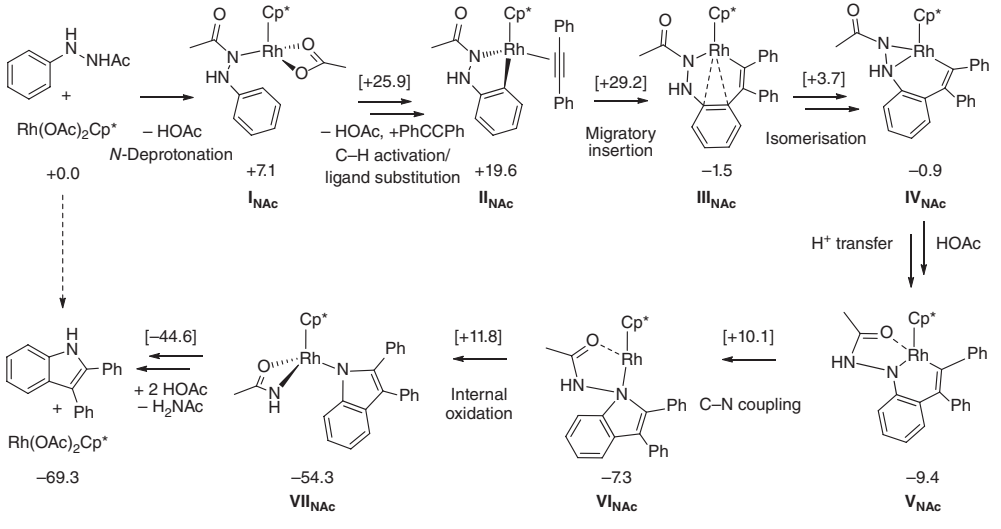

Figure 1.32 Key stationary points on free energy profiles (kcal mol^{-1}) for the $Rh(OAc)_2Cp^*$-catalyzed reaction of 2-acetyl-1-arylhydrazines with diphenylacetylene to give indoles [81]. Double arrows indicate several steps are involved, with the energy of the highest transition state between the two minima indicated in square brackets.

In contrast to previous pathways, no Rh(V) species are invoked in this process, but rather a Rh(III)–Rh(I)–Rh(III) pathway is proposed. Experimentally, the reaction proceeds at 70 °C [82] and a k_H/k_D KIE of 2.3 is observed. The rate-limiting alkyne insertion implied by the calculations therefore appears inconsistent with this; however, an endothermic (i.e., reversible) initial C–H activation step would also be expected to affect the overall rate [83]. The use of kinetic simulations to quantify these effects would be of interest. Calculations comparing the –NH(NHOAc) and –NH(OAc) groups suggest the former is a weaker oxidant that can promote C–N bond coupling with alkynes but not with alkenes.

1.3.3.2 Heterocycle Formation without Internal Oxidants

Davies, Macgregor, and coworkers have studied the $Rh(OAc)_2Cp^*$-catalyzed oxidative coupling of 5-methyl-3-phenylpyrazole and 4-octyne with BP86(DCE) and BP86-D3(DCE) calculations (Figure 1.33) [84]. Experimental H/D exchange studies indicate reversible C–H activation both in the absence (40% *ortho*-deuteration) and in the presence of the alkyne (7% incorporation). This indicates close competition between protonolysis of the initial cyclometalated intermediate, **II** (via **TS(I–II)**), and the onward reaction involving HOAc/alkyne substitution and migratory insertion (via **TS(III–IV)**). This competition was only correctly reproduced when the D3 dispersion correction was employed and primarily reflects changes in the HOAc/^{n}PrCC^{n}Pr substitution step (ΔG_{calc}:

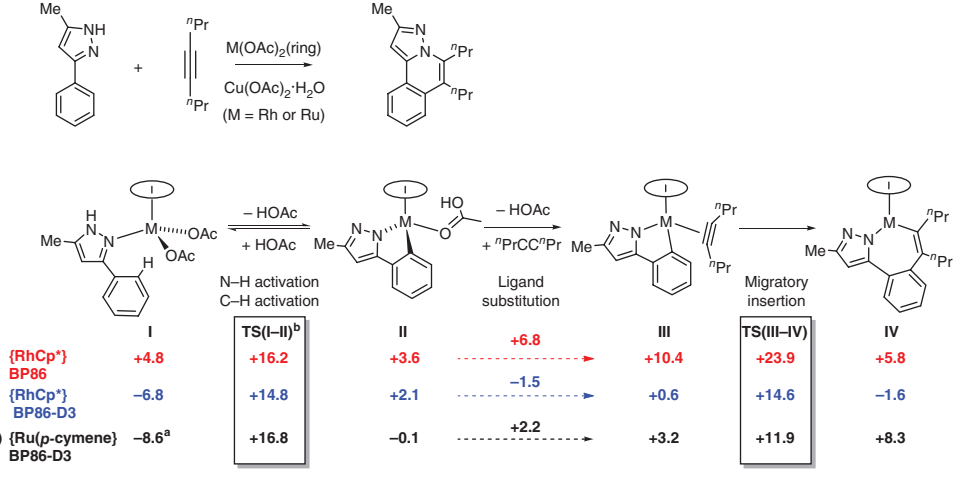

Figure 1.33 (a) Rh- and Ru-catalyzed oxidative coupling of 5-methyl-3-phenylpyrazole and 4-octyne to form a pyrazoloisoquinoline. (b) Key stationary points on the free energy profiles (kcal mol^{-1}) for (i) {RhCp*} (BP86(DCE), red), (ii) {RhCp*} (BP86-D3(DCE), blue), and (iii) {Ru(*p*-cymene)} (BP86-D3(MeOH), black), quoted relative to reactants set to 0.0 kcal mol^{-1} in each case 84. [a]8.6 kcal mol^{-1} corresponds to the lowest point on the profile and is the N–H-activated form of **I**. [b]The formation of **II** from **I** involves several steps and **TS(I–II)** is the highest point in this process.

BP86 = +6.8 kcal mol^{-1}; BP86-D3 = −1.5 kcal mol^{-1}). This is particularly sensitive to dispersion effects because of the different bulk of the two ligands involved. Alternative methods that include a treatment of dispersion effects (e.g., M06 or B97-D, or addition of the D3 correction to other pure and hybrid functionals) also performed well in this regard.

Comparison with the Ru(OAc)$_2$(*p*-cymene) catalyst proved instructive. For both metals, rate-limiting C–H activation was computed, with a higher barrier for Ru (25.4 kcal mol^{-1}) compared to Rh (21.8 kcal mol^{-1}). This is consistent with the higher temperature required for Ru experimentally (2-methylbutanol, 120 °C cf. DCE at 83 °C for Rh). For Rh, an observed k_H/k_D KIE of 2.7 ± 0.5 is consistent with the computed two-step C–H activation where the higher transition state, **TS(I–II)$_{Rh}$** (Figure 1.34), corresponds to C–H bond cleavage occurring after an agostic intermediate (a calculated KIE based on **TS(I–II)$_{Rh}$** was 5.5). In contrast, the observed k_H/k_D KIE at Ru was small (1.1 ± 0.2). In this case, however, calculations indicated a one-step C–H activation via **TS(I–II)$_{Ru}$**, which equates to the κ^2–κ^1 displacement of OAc. **TS(I–II)$_{Ru}$** therefore features minimal C–H bond elongation and the computed KIE is only 1.2, in good agreement with experiment. An important conclusion from this study is that the lack of a significant k_H/k_D KIE does not *necessarily* mean that C–H activation is not rate limiting; it may simply be that the C–H activation has a very early transition state geometry.

Lledós, Urriolabeitia, and coworkers have used M06(MeOH) calculations to model the oxidative coupling of benzylamines with 2-butyne at [Ru(Cl)$_2$(*p*-cymene)]$_2$ (Figure 1.35) [85]. The presence of protic N–H bonds in benzylamine promotes the formation of H-bonded ion pairs upon OAc dissociation, and these proved more reactive than non-ion-paired species where OAc was modeled as fully dissociated in solution. Thus, after OAc/amine substitution at Ru(OAc)$_2$(*p*-cymene) to give **I·OAc**, an outer-sphere C–H activation is computed via a transition state at 24.6 kcal mol^{-1}, 2.5 kcal mol^{-1} below a more conventional intramolecular process. Although this external deprotonation cannot strictly

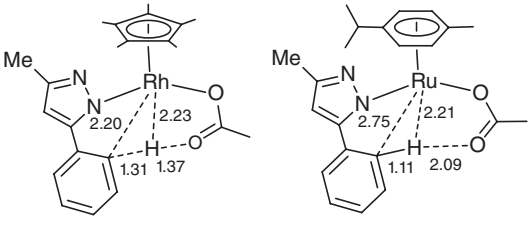

k_H/k_D (exp) = 2.7 ± 0.5
k_H/k_D (calc) = 5.5
TS(I–II)$_{Rh}$

k_H/k_D (exp) = 1.1 ± 0.2
k_H/k_D (calc) = 1.2
TS(I–II)$_{Ru}$

Figure 1.34 Rate-limiting transition states with key distances (Å) for the C–H activation of 5-methyl-3-phenylpyrazole at {Rh(OAc)Cp*} (**TS(I–II)$_{Rh}$**) and {Ru(OAc)(*p*-cymene)} (**TS(I–II)$_{Ru}$**). Associated experimental and computed k_H/k_D KIE data are also shown [84].

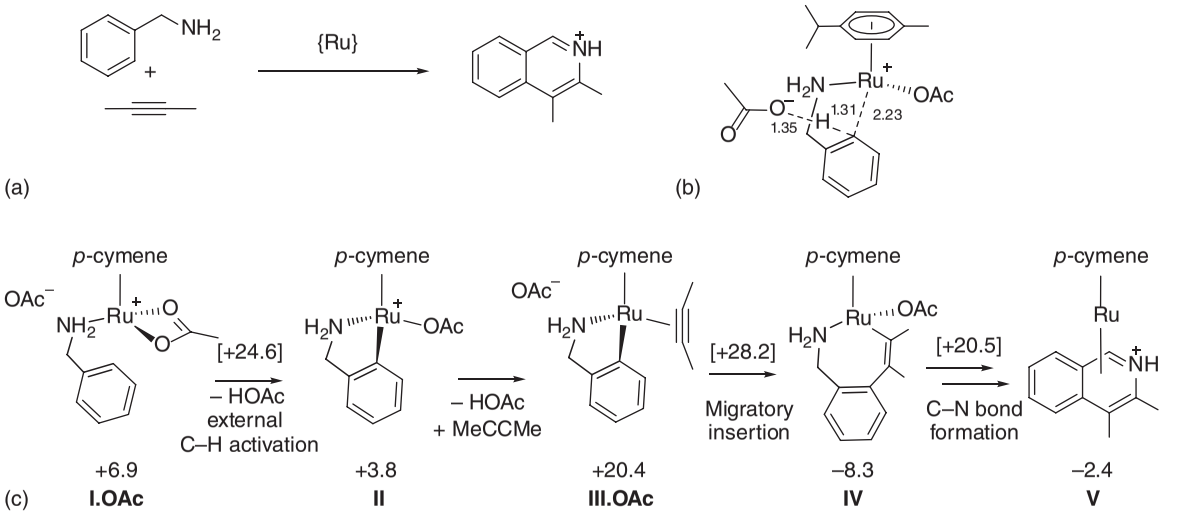

Figure 1.35 (a) Ru-catalyzed oxidative coupling of benzylamines with 2-butyne to form isoquinolones; (b) transition state for C–H activation via external deprotonation with key distances (Å); and (c) key stationary points on the free energy profile (kcal mol^{-1}; energies quoted relative to the reactants at 0.0 kcal mol^{-1}). Double arrows indicate several steps are involved, with the energy of the highest transition state between the two minima indicated in square brackets [85].

be termed *AMLA* (as this implies a coordinated ligand acting as a base), it does display some common features, namely, the interaction of the C–H bond with an electron-deficient metal center which activates it to deprotonation by a base. "CMD" would describe this concerted process appropriately. After loss of HOAc, OAc/MeCCMe substitution gives a further ion pair, **III·OAc**, that undergoes insertion to a seven-membered ruthenacycle, which is then trapped by OAc to form a saturated intermediate, **IV**. Of several routes considered for C–N bond formation, a process involving *N*-decoordination and nucleophilic attack of the free amine arm at the bound Ru-alkenyl moiety was found to be most accessible, with an overall barrier relative to **IV** of 28.8 kcal mol^{-1}; OAc is again H bonded to the amine during this process. The protonated 1,2-dihydroisoquinoline is thus formed bound to a Ru(0) metal center (**V**). Overall, no clear rate-determining process could be identified, with insertion and C–N bond formation both having similar barriers of about 29 kcal mol^{-1}, both slightly higher than C–H activation. Experimentally, temperatures of about 100 °C are required. Related profiles were computed for 1-naphthylmethyl, 2-methylallylamine, and 2-thiophenemethylamine.

The Ir(OAc)$_2$Cp*-catalyzed oxidative coupling of benzoic acids with alkynes has been studied with BP86(MeOH) calculations by Ison and coworkers (Figure 1.36a) [86]. These confirmed the previously reported result [58a] that C–H activation proceeds via acetate assistance and not OA. The subsequent insertion of 4-octyne insertion is thought to be rate limiting and has a transition state at +29.6 kcal mol^{-1}. This is perhaps rather high for a reaction that completes after 1 h at 60 °C, and it would be interesting to see how this barrier would be affected by a treatment of dispersion effects. After insertion, C–O reductive coupling then gives the isocoumarin product bound as an η^4-ligand at an Ir(I) center. Oxidation via reaction with AgOAc to give an Ir(II)OAc intermediate (and a Ag atom) is proposed to be necessary to release the organic product, with reaction with a second equivalent of AgOAc then regenerating the Ir(III)(OAc)$_2$ catalyst.

The related synthesis of phosphaisocoumarins via the Rh-catalyzed coupling of phenylphosphonates and alkynes (Figure 1.36b) was modeled by Zhao and coworkers with B3LYP-D3(^{t}BuOH) calculations [87]. Using a model system (Rh(OAc)$_2$Cp, PhP(O)(OMe)(OH), and 2-butyne), the authors defined a pathway with an energy span [88] of 36.8 kcal mol^{-1}, which increases to 50.2 kcal mol^{-1} if

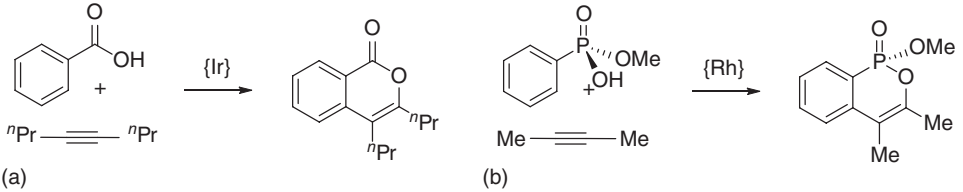

Figure 1.36 (a) Ir-catalyzed isocoumarin formation [86] and (b) Rh-catalyzed phosphaisocoumarin formation [87].

a low-energy carbonate intermediate, $Rh(CO_3)Cp\{PhP(O)(OMe)(OH)\}$, is taken into account. The computed rate-limiting transition state involves C–C coupling. It is difficult to reconcile these computed results with a process that operates efficiently at 90 °C and has an observed k_H/k_D KIE of 5.3 [89]. Use of a truncated model was addressed with tests comparing Cp and Cp* and gave similar results for the rate-limiting C–C coupling. However, these were performed with 2-butyne, an alkyne that is not used experimentally. The importance of combining the full steric bulk of all substrates and catalysts to construct a reasonable model has already been stressed [84].

1.3.4 Alkenylation and Amination

The first computational contribution to this area came from Huang, Fu, and coworkers with their 2013 study of Rh(III)-catalyzed oxidative Heck coupling of phenol carbamates with alkenes (see Figure 1.37) [90]. Using an M06(THF)//B3LYP protocol, they modeled the reaction of *m*-tolyldimethylcarbamate with ethyl acrylate at $[Rh(OAc)Cp^*]^+$, supported by preliminary work on a Cp model. An initial adduct formed via the carbamate oxygen (**I**, 0.0 kcal mol^{-1}) provides access to a one-step C–H activation at the less hindered *ortho* position with a barrier of 22.2 kcal mol^{-1} to give, after loss of HOAc, a six-membered metalacycle, **II**, at +7.9 kcal mol^{-1}. Ethyl acrylate can then undergo 2,1-insertion into the Rh–C bond with an overall barrier of 11.9 kcal mol^{-1} resulting in an eight-membered rhodacycle, **III**, at *−5.5* kcal mol^{-1}. β-H transfer is then uphill ($\Delta G^{\ddagger} = 16.9$ kcal mol^{-1}; $\Delta G = +16.8$ kcal mol^{-1}), but it is assumed that the Rh(I)-H intermediate, **IV**, can then release the coupled product in the presence of $Cu(OAc)_2$ oxidant. C–H activation is therefore computed to be rate limiting, consistent with an intramolecular k_H/k_D KIE of 3.1. Experimentally, the modeled reaction requires 24 h at 110 °C [91]. An alternative mechanism based on initial

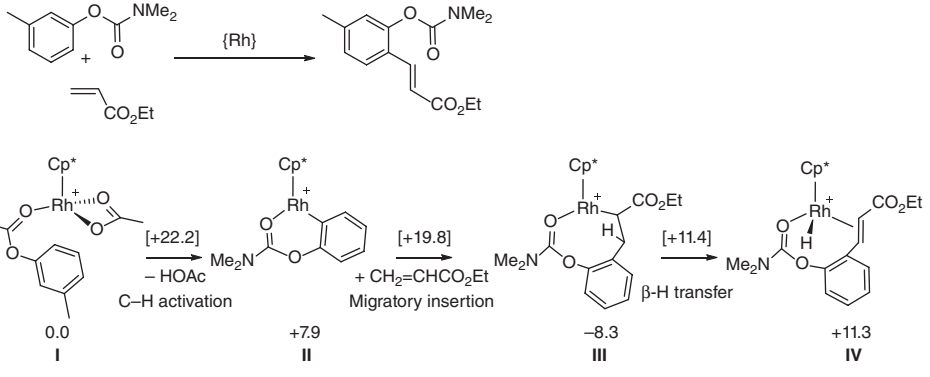

Figure 1.37 (a) Rh-catalyzed alkenylation of *m*-tolyldimethylcarbamate with ethyl acrylate and (b) key stationary points on the free energy profile (kcal mol^{-1}; energies quoted relative to the reactants at 0.0 kcal mol^{-1}) [90].

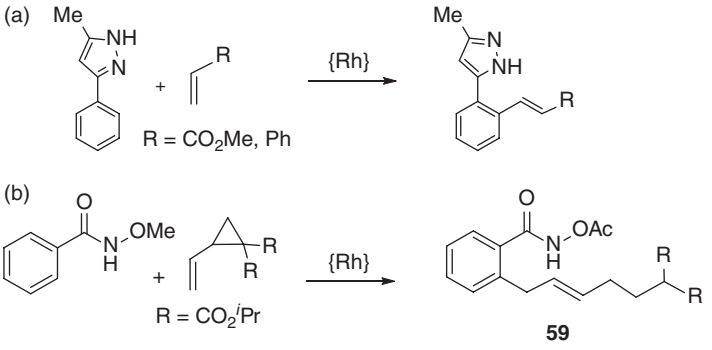

Figure 1.38 Rh-catalyzed alkenylation reactions: (a) 3-phenylpyrazole with $H_2C{=}CHR$ (R = Ph, CO_2Me) [92] and (b) *N*-methoxybenzamide with dimethyl-2-vinylcyclopropane-1,1-dicarboxylate [93].

C–H activation of ethyl acrylate was also considered and found to have a higher barrier of 25.1 kcal mol^{-1}.

The related coupling of 5-methyl-3-phenylpyrazole with both methyl acrylate and styrene at $Rh(OAc)_2Cp^*$ was modeled by Davies, Macgregor, and coworkers using a BP86-D3(DCE) method (Figure 1.38a) [92]. Starting from alkene adducts of their previously computed cyclometalated intermediate [84], a clear preference for 2,1-insertion was computed for both alkenes, with barriers of about 20 kcal mol^{-1} for methyl acrylate and about 23 kcal mol^{-1} for styrene. Insertion produces conformationally flexible rhodacycles from which β-H transfer to both the *cis* and *trans* alkene products was characterized, with formation of the *trans* isomers being both kinetically and thermodynamically favored. Overall, for methyl acrylate, similar barriers for insertion and the preceding C–H activation were computed, whereas the higher insertion barrier for styrene makes this process rate limiting in this case. Using M06(CF_3CH_2OH) calculations, Huang, Wang, and coworkers showed that the reaction of dimethyl-2-vinylcyclopropane-1,1-dicarboxylate with *N*-methoxybenzamide (Figure 1.38b) proceeds via rate-limiting 2,1-insertion with an overall barrier of 26.1 kcal mol^{-1}. This is preceded by a reversible C–H activation with a barrier of 21.4 kcal mol^{-1} [93]. Experimentally, a small k_H/k_D KIE of 1.7 was obtained from a parallel experiment. In this case, subsequent β-H elimination and ring opening of the pendant cyclopropane moiety gives access to a highly functionalized (*E*)-but-2-en-1-yl-dimethylmalonate moiety, **59**.

The direct C–H amination of *N-tert*-butylbenzamide with organic azides catalyzed by Gp 9 $M(OAc)_2Cp^*$ species has been modeled by Chang, Musaev, and coworkers with M06(DCE) calculations (Figure 1.39) [94]. Experimentally, $[MCl_2Cp^*]_2$ precatalysts are employed along with an $AgSbF_6$ additive, and the latter is assumed to effect the necessary C–H activation (presumably via an EA mechanism, i.e., without any specific base assistance) to arrive at a $[M(BA)Cp]^+$ intermediate (where BA is an *O*-bound, C–H-activated *N-tert*-butylbenzamide ligand). The reaction proceeds by coordination of PhN_3 followed by loss of N_2 to

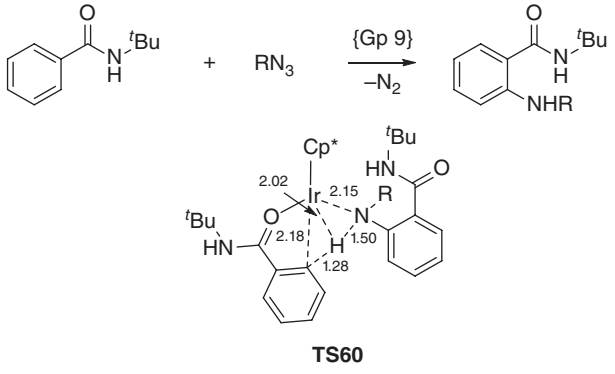

Figure 1.39 Gp 9-catalyzed amination of *N-tert*-butylbenzamide with organic azides, along with the structure of the AMLA-4 C–H activation transition state, **TS60**, with key distances in Å.

form a M(V) nitrene that can then insert into the M–C bond. Protodemetalation then proceeds via C–H activation of the benzamide substrate, in which the amido nitrogen acts as an internal base (an AMLA-4 step; see **TS60**, Figure 1.39). This releases the amination product and regenerates the $[M(BA)Cp]^+$ active species. When M = Rh, significant barriers are computed for N_2 loss (30.9 kcal mol^{-1}) and the final C–H activation step (40.6 kcal mol^{-1}). The equivalent barriers for Ir are 29.5 and 33.9 kcal mol^{-1}, respectively, with the reduced barriers to C–H activation arising from enhanced charge density on the nitrene nitrogen in this case. Experimentally, the Ir system is more promising with the reaction of ArN_3 (Ar = 3,5-$(CF_3)_2C_6H_3$) proceeding in 47% yield (90 min, 65 °C); in contrast, Rh gives an 8% yield under these conditions. A significant k_H/k_D KIE is seen observed for the Ir system and $\Delta H^{\ddagger}_{exp}$ is 20.3 kcal mol^{-1}, in reasonable agreement with the computed value of 17.9 kcal mol^{-1}. In contrast, the small value of $\Delta S^{\ddagger}_{exp}$ (1.4 cal mol^{-1} K^{-1}) is at odds with the strongly associative mechanism implied computationally. For the Co(III) analog, barriers of 31.7 kcal mol^{-1} (N_2 loss) and 51.9 kcal mol^{-1} (C–H activation) are computed, and indeed the Co system is an ineffective catalyst experimentally.

1.4 Conclusions

This chapter has surveyed the contribution of computational chemistry in understanding the mechanisms of heteroatom-assisted C–H bond activations at Pd as well as Ru, Rh, and Ir metal centers. The underlying basis of these processes is now well understood with the combination of an electron-deficient metal center and a chelating base providing a powerful means to cleave C–H bonds, especially when a directing group is employed to facilitate this process. Intermolecular C–H activation of (hetero)arenes is now well documented, particularly at Pd(II) where the

CMD concept has provided significant insight into both activities and selectivities. This process is now being exploited in Pd-catalyzed direct arylation chemistry and is proving an effective means to produce functionalized heterocycles. Challenges in the mechanistic understanding of such processes still remain, however, not least in defining the true nature of the Pd active species and the role of additives. Intramolecular C–H activation in the presence of a directing group is providing the basis for heterocycle synthesis via oxidative coupling reactions, particularly with alkynes and alkenes, and most commonly at Rh(III). The computation of full catalytic cycles based on C–H activation and functionalization is becoming more prevalent, and the discipline is well placed to play an active role in furthering efforts in this area. In doing so, the use of more realistic models that better reflect the systems used experimentally will be important, and this is made possible by the availability of increased computational power. However, such models bring with them the dual challenges of a correct treatment of weak interactions and an assessment of conformational flexibility. Close interaction with experiment is still vital in order to benchmark computational protocols against experimental data, and the most valuable studies in this chapter have been based on a close alignment of experiment and computation. Improved mechanistic insight therefore demands input from experiment in the form of quantitative experimental data, while computational chemists must be stringent in testing their methods against such data. With this approach, the role of computation in integrating C–H activation into ever-more ambitious catalytic schemes has a vibrant future.

Acknowledgments

We thank Prof Dai Davies (University of Leicester) and his group for many fruitful discussions and the EPSRC for financial support through awards EP/J002712/1 (KJTC) and EP/J021911/1 (CLM).

References

1. (a) Balcells, D., Clot, E., and Eisenstein, O. (2010) *Chem. Rev.*, **110**, 749–823; (b) Boutadla, Y., Davies, D.L., Macgregor, S.A., and Poblador-Bahamonde, A.I. (2009) *Dalton Trans.*, 5820–5831; (c) Perutz, R.N. and Sabo-Etienne, S. (2007) *Angew. Chem. Int. Ed.*, **46**, 2578–2592; (d) Vastine, B.A. and Hall, M.B. (2009) *Coord. Chem. Rev.*, **253**, 1202–1218; (e) Lapointe, D. and Fagnou, K. (2010) *Chem. Lett.*, **39**, 1119–1126.
2. For recent related reviews see: (a) Guan, W., Sayyed, F.B., Zeng, G., and Sakaki, S. (2014) *Inorg. Chem.*, **53**, 6444–6457; (b) Pahls, D.R., Allen, K.E., Goldberg, K.I., and Cundari, T.R. (2014) *Organometallics*, **33**, 6413–6419.
3. Grimme, S., Antony, J., Ehrlich, S., and Krieg, H. (2010) *J. Chem. Phys.*, **132**, 154104.
4. Grimme, S. (2006) *J. Comput. Chem.*, **27**, 1787–1799.
5. Chai, J.-D. and Head-Gordon, M. (2008) *Phys. Chem. Chem. Phys.*, **10**, 6615–6620.
6. Zhao, Y. and Truhlar, D. (2008) *Theor. Chem. Acc.*, **120**, 215–241.
7. Minenkov, Y., Occhipinti, G., and Jensen, V.R. (2009) *J. Phys. Chem. A*, **113**, 11833–11844.

8. Davies, D.L., Donald, S.M.A., and Macgregor, S.A. (2005) *J. Am. Chem. Soc.*, **127**, 13754–13755.
9. Ryabov, A.D., Sakodinskaya, I.K., and Yatsimirsky, A.K. (1985) *J. Chem. Soc., Dalton Trans.*, 2629–2638.
10. García-Cuadrado, D., de Mendoza, P., Braga, A.A.C., Maseras, F., and Echavarren, A.M. (2007) *J. Am. Chem. Soc.*, **129**, 6880–6886.
11. García-Cuadrado, D., Braga, A.A.C., Maseras, F., and Echavarren, A.M. (2006) *J. Am. Chem. Soc.*, **128**, 1066–1067.
12. Lafrance, M., Gorelsky, S.I., and Fagnou, K. (2007) *J. Am. Chem. Soc.*, **129**, 14570–14571.
13. Aguilar, D., Bielsa, R., Contel, M., Lledós, A., Navarro, R., Soler, T., and Urriolabeitia, E.P. (2008) *Organometallics*, **27**, 2929–2936.
14. Chaumontet, M., Piccardi, R., Audic, N., Hitce, J., Peglion, J.-L., Clot, E., and Baudoin, O. (2008) *J. Am. Chem. Soc.*, **130**, 15157–15166.
15. Kefalidis, C.E., Baudoin, O., and Clot, E. (2010) *Dalton Trans.*, **39**, 10528–10535.
16. Rousseaux, S., Davi, M., Sofack-Kreutzer, J., Pierre, C., Kefalidis, C.E., Clot, E., Fagnou, K., and Baudoin, O. (2010) *J. Am. Chem. Soc.*, **132**, 10706–10716.
17. Häller, L.J.L., Page, M.J., Macgregor, S.A., Mahon, M.F., and Whittlesey, M.K. (2009) *J. Am. Chem. Soc.*, **131**, 4604–4605.
18. Rousseaux, S., Gorelsky, S.I., Chung, B.K.W., and Fagnou, K. (2010) *J. Am. Chem. Soc.*, **132**, 10692–10705.
19. Aullón, G., Chat, R., Favier, I., Font-Bardia, M., Gómez, M., Granell, J., Martínez, M., and Solans, X. (2009) *Dalton Trans.*, 8292–8300.
20. Anand, M. and Sunoj, R.B. (2012) *Organometallics*, **31**, 6466–6481.
21. Dang, Y., Qu, S., Nelson, J.W., Pham, H.D., Wang, Z.-X., and Wang, X. (2015) *J. Am. Chem. Soc.*, **137**, 2006–2014.
22. Cheng, G.-J., Yang, Y.-F., Liu, P., Chen, P., Sun, T.-Y., Li, G., Zhang, X., Houk, K.N., Yu, J.-Q., and Wu, Y.-D. (2014) *J. Am. Chem. Soc.*, **136**, 894–897.
23. Yang, Y.-F., Cheng, G.-J., Liu, P., Leow, D., Sun, T.-Y., Chen, P., Zhang, X., Yu, J.-Q., Wu, Y.-D., and Houk, K.N. (2014) *J. Am. Chem. Soc.*, **136**, 344–355.
24. Yoo, E.J., Ma, S., Mei, T.S., Chan, K.S.L., and Yu, J.Q. (2011) *J. Am. Chem. Soc.*, **133**, 7652–7655.
25. Anand, M., Sunoj, R.B., and Schaefer, H.F. III, (2014) *J. Am. Chem. Soc.*, **136**, 5535–5538.
26. (a) Musaev, D.G., Figg, T.M., and Kaledin, A.L. (2014) *Chem. Soc. Rev.*, **43**, 5009–5031; (b) Figg, T.M., Wasa, M., Yu, J.-Q., and Musaev, D.G. (2013) *J. Am. Chem. Soc.*, **135**, 14206–14214.
27. Roiban, G.-D., Serrano, E., Soler, T., Aullón, G., Grosu, I., Cativiela, C., MartÍnez, M., and Urriolabeitia, E.P. (2011) *Inorg. Chem.*, **50**, 8132–8143.
28. Cross, W.B., Hope, E.G., Lin, Y.-H., Macgregor, S.A., Singh, K., Solan, G.A., and Yahya, N. (2013) *Chem. Commun.*, **49**, 1918–1920.
29. Chen, F.-J., Zhao, S., Hu, F., Chen, K., Zhang, Q., Zhang, S.-Q., and Shi, B.-F. (2013) *Chem. Sci.*, **4**, 4187–4192.
30. Giri, R., Lan, Y., Liu, P., Houk, K.N., and Yu, J.-Q. (2012) *J. Am. Chem. Soc.*, **134**, 14118–14126.
31. (a) Katayev, D., Larionov, E., Nakanishi, M., Besnard, C., and Kündig, E.P. (2014) *Chem. Eur. J.*, **20**, 15021–15030; (b) Larionov, E., Nakanishi, M., Katayev, D., Besnard, C., and Kündig, E.P. (2013) *Chem. Sci.*, **4**, 1995–2005.
32. Biswas, B., Sugimoto, M., and Sakaki, S. (2000) *Organometallics*, **19**, 3895–3908.
33. Lafrance, M., Rowley, C.N., Woo, T.K., and Fagnou, K. (2006) *J. Am. Chem. Soc.*, **128**, 8754–8756.
34. Lafrance, M. and Fagnou, K. (2006) *J. Am. Chem. Soc.*, **128**, 16496–16497.
35. Gorelsky, S.I., Lapointe, D., and Fagnou, K. (2008) *J. Am. Chem. Soc.*, **130**, 10848–10849.
36. Lapointe, D., Markiewicz, T., Whipp, C.J., Toderian, A., and Fagnou, K. (2011) *J. Org. Chem.*, **76**, 749–759.
37. (a) Gorelsky, S.I., Lapointe, D., and Fagnou, K. (2012) *J. Org. Chem.*, **77**, 658–668; (b) Gorelsky, S.I. (2013) *Coord. Chem. Rev.*, **257**, 153–164; (c) Gorelsky, S.I. (2012) *Organometallics*, **31**, 794–797.
38. van Zeist, W.-J. and Bickelhaupt, F.M. (2010) *Org. Biomol. Chem.*, **8**, 3118–3127.

39. Guihaumé, J., Clot, E., Eisenstein, O., and Perutz, R.N. (2010) *Dalton Trans.*, **39**, 10510–10519.
40. Petit, A., Flygare, J., Miller, A.T., Winkel, G., and Ess, D.H. (2012) *Org. Lett.*, **14**, 3680–3683.
41. Liégault, B., Petrov, I., Gorelsky, S.I., and Fagnou, K. (2010) *J. Org. Chem.*, **75**, 1047–1060.
42. Wakioka, M., Nakamura, Y., Hihara, Y., Ozawa, F., and Sakaki, S. (2014) *Organometallics*, **33**, 6247–6252.
43. (a) Yanagisawa, S., Ueda, K., Sekizawa, H., and Itami, K. (2009) *J. Am. Chem. Soc.*, **131**, 14622–14623; (b) Ueda, K., Yanagisawa, S., Yamaguchi, J., and Itami, K. (2010) *Angew. Chem. Int. Ed.*, **49**, 8946–8949.
44. Steinmetz, M., Ueda, K., Grimme, S., Yamaguchi, J., Kirchberg, S., Itami, K., and Studer, A. (2012) *Chem. Asian J.*, **7**, 1256–1260.
45. Tang, S.-Y., Guo, Q.-X., and Fu, Y. (2011) *Chem. Eur. J.*, **17**, 13866–13876.
46. Cong, X., Tang, H., Wu, C., and Zeng, X. (2013) *Organometallics*, **32**, 6565–6575.
47. Zhang, S., Shi, L., and Ding, Y. (2011) *J. Am. Chem. Soc.*, **133**, 20218–20229.
48. Campeau, L.-C., Bertrand-Laperle, M., Leclerc, J.-P., Villemure, E., Gorelsky, S., and Fagnou, K. (2008) *J. Am. Chem. Soc.*, **130**, 3276–3277.
49. Potavathri, S., Pereira, K.C., Gorelsky, S.I., Pike, A., LeBris, A.P., and DeBoef, B. (2010) *J. Am. Chem. Soc.*, **132**, 14676–14681.
50. Ishikawa, A., Nakao, Y., Sato, H., and Sakaki, S. (2010) *Dalton Trans.*, **39**, 3279–3289.
51. Sanhueza, I.A., Wagner, A.M., Sanford, M.S., and Schoenebeck, F. (2013) *Chem. Sci.*, **4**, 2767–2775.
52. Xi, P., Yang, F., Qin, S., Zhao, D., Lan, J., Gao, G., Hu, C., and You, J. (2010) *J. Am. Chem. Soc.*, **132**, 1822–1824.
53. Meir, R., Kozuch, S., Uhe, A., and Shaik, S. (2011) *Chem. Eur. J.*, **17**, 7623–7631.
54. Tan, Y. and Hartwig, J.F. (2011) *J. Am. Chem. Soc.*, **133**, 3308–3311.
55. Sun, H.-Y., Gorelsky, S.I., Stuart, D.R., Campeau, L.-C., and Fagnou, K. (2010) *J. Org. Chem.*, **75**, 8180–8189.
56. Tan, Y., Barrios-Landeros, F., and Hartwig, J.F. (2012) *J. Am. Chem. Soc.*, **134**, 3683–3686.
57. Stephens, D.E., Lakey-Beitia, J., Atesin, A.C., Ateşin, T.A., Chavez, G., Arman, H.D., and Larionov, O.V. (2015) *ACS Catal.*, **5**, 167–175.
58. (a) Davies, D.L., Donald, S.M.A., Al-Duaij, O., Macgregor, S.A., and Polleth, M. (2006) *J. Am. Chem. Soc.*, **128**, 4210–4211; (b) Boutadla, Y., Davies, D.L., Macgregor, S.A., and Poblador-Bahamonde, A.I. (2009) *Dalton Trans.*, 5887–5893.
59. Davies, D.L., Donald, S.M.A., Al-Duaij, O., Fawcett, J., Little, C., and Macgregor, S.A. (2006) *Organometallics*, **25**, 5976–5978.
60. Özdemir, I., Demir, S., Çetinkaya, B., Gourlaouen, C., Maseras, F., Bruneau, C., and Dixneuf, P.H. (2008) *J. Am. Chem. Soc.*, **130**, 1156–1157.
61. Carr, K.J.T., Davies, D.L., Macgregor, S.A., Singh, K., and Villa-Marcos, B. (2014) *Chem. Sci.*, **5**, 2340–2346.
62. Li, J., Hu, W., Peng, Y., Zhang, Y., Li, J., and Zheng, W. (2014) *Organometallics*, **33**, 2150–2159.
63. Li, L., Brennessel, W.W., and Jones, W.D. (2009) *Organometallics*, **28**, 3492–3500.
64. Clot, E., Eisenstein, O., Jasim, N., Macgregor, S.A., McGrady, J.E., and Perutz, R.N. (2011) *Acc. Chem. Res.*, **44**, 333–348.
65. Davies, D.L., Macgregor, S.A., and Poblador-Bahamonde, A.I. (2010) *Dalton Trans.*, **39**, 10520–10527.
66. Ess, D.H., Bischof, S.M., Oxgaard, J., Periana, R.A., and Goddard, W.A. III, (2008) *Organometallics*, **27**, 6440–6445.
67. García-Melchor, M., Gorelsky, S.I., and Woo, T.K. (2011) *Chem. Eur. J.*, **17**, 13847–13853.
68. Oxgaard, J., Tenn, W.J. III, Nielsen, R.J., Periana, R.A., and Goddard, W.A. III, (2007) *Organometallics*, **26**, 1565–1567.
69. Oxgaard, J., Muller, R.P., Goddard, W.A., and Periana, R.A. (2004) *J. Am. Chem. Soc.*, **126**, 352–363.
70. Cundari, T.R., Grimes, T.V., and Gunnoe, T.B. (2007) *J. Am. Chem. Soc.*, **129**, 13172–13182.
71. (a) Meier, S.K., Young, K.J.H., Ess, D.H., Tenn, W.J. III, Oxgaard, J., Goddard,

W.A. III, and Periana, R.A. (2009) *Organometallics*, **28**, 5293–5304; (b) Bischof, S.M., Ess, D.H., Meier, S.K., Oxgaard, J., Nielsen, R.J., Bhalla, G., Goddard, W.A. III, and Periana, R.A. (2010) *Organometallics*, **29**, 742–756.

72. Webster-Gardiner, M.S., Fu, R., Fortman, G.C., Nielsen, R.J., Gunnoe, T.B., and Goddard, W.A. III, (2015) *Catal. Sci. Technol.*, **5**, 96–100.
73. Rhinehart, J.L., Manbeck, K.A., Buzak, S.K., Lippa, G.M., Brennessel, W.W., Goldberg, K.I., and Jones, W.D. (2012) *Organometallics*, **31**, 1943–1952.
74. Cross, W.B., Razak, S., Singh, K., and Warner, A.J. (2014) *Chem. Eur. J.*, **20**, 13203–13209.
75. Guimond, N., Gorelsky, S.I., and Fagnou, K. (2011) *J. Am. Chem. Soc.*, **133**, 6449–6457.
76. Xu, L., Zhu, Q., Huang, G., Cheng, B., and Xia, Y. (2012) *J. Org. Chem.*, **77**, 3017–3024.
77. Wodrich, M.D., Ye, B., Gonthier, J.F., Corminboeuf, C., and Cramer, N. (2014) *Chem. Eur. J.*, **20**, 15409–15418.
78. Wu, S., Zeng, R., Fu, C., Yu, Y., Zhang, X., and Ma, S. (2015) *Chem. Sci.*, **6**, 2275–2285.
79. Xing, Z., Huang, F., Sun, C., Zhao, X., Liu, J., and Chen, D. (2015) *Inorg. Chem.*, **54**, 3958–3969.
80. Yu, S., Liu, S., Lan, Y., Wan, B., and Li, X. (2015) *J. Am. Chem. Soc.*, **137**, 1623–1631.
81. Chen, W.-J. and Lin, Z. (2015) *Organometallics*, **34**, 309–318.
82. Zhao, D., Shi, Z., and Glorius, F. (2013) *Angew. Chem. Int. Ed.*, **52**, 12426–12429.
83. Simmons, E.M. and Hartwig, J.F. (2012) *Angew. Chem. Int. Ed.*, **51**, 3066–3072.
84. Algarra, A.G., Cross, W.B., Davies, D.L., Khamker, Q., Macgregor, S.A., McMullin, C.L., and Singh, K. (2014) *J. Org. Chem.*, **79**, 1954–1970.
85. Ruiz, S., Villuendas, P., Ortuño, M.A., Lledós, A., and Urriolabeitia, E.P. (2015) *Chem. Eur. J.*, **21**, 8626–8636.
86. Frasco, D.A., Lilly, C.P., Boyle, P.D., and Ison, E.A. (2013) *ACS Catal.*, **3**, 2421–2429.
87. Liu, L., Wu, Y., Wang, T., Gao, X., Zhu, J., and Zhao, Y. (2014) *J. Org. Chem.*, **79**, 5074–5081.
88. Kozuch, S. and Shaik, S. (2011) *Acc. Chem. Res.*, **44**, 101–110.
89. (a) Park, Y., Seo, J., Park, S., Yoo, E.J., and Lee, P.H. (2013) *Chem. Eur. J.*, **19**, 16461–16468; (b) Seo, J., Park, Y., Jeon, I., Ryu, T., Park, S., and Lee, P.H. (2013) *Org. Lett.*, **15**, 3358–3361.
90. Zhang, Q., Yu, H.-Z., Li, Y.-T., Liu, L., Huang, Y., and Fu, Y. (2013) *Dalton Trans.*, **42**, 4175–4184.
91. Gong, T.-J., Xiao, B., Liu, Z.-J., Wan, J., Xu, J., Luo, D.-F., Fu, Y., and Liu, L. (2011) *Org. Lett.*, **13**, 3235–3237.
92. Algarra, A.G., Davies, D.L., Khamker, Q., Macgregor, S.A., McMullin, C.L., Singh, K., and Villa-Marcos, B. (2015) *Chem. Eur. J.*, **21**, 3087–3096.
93. Wu, J.-Q., Qiu, Z.-P., Zhang, S.-S., Liu, J.-G., Lao, Y.-X., Gu, L.-Q., Huang, Z.-S., Li, J., and Wang, H. (2015) *Chem. Commun.*, **51**, 77–80.
94. Figg, T.M., Park, S., Park, J., Chang, S., and Musaev, D.G. (2014) *Organometallics*, **33**, 4076–4085.